

# Geochemistry, Geophysics, Geosystems®



## RESEARCH ARTICLE

10.1029/2021GC009781

### Key Points:

- Ridge-hotspot interactions were tracked via the isotopic composition of basalts sampled across the East Pacific Rise axis
- Chronological reconstructions of collected mid-ocean ridge basalts reveal a periodicity of 125 kyrs in the recorded isotopic signal
- High-resolution sampling allows the integration of geochemical information within the framework of geophysical and geological models

### Supporting Information:

Supporting Information may be found in the online version of this article.

### Correspondence to:

B. Mougel,  
[mougel@geociencias.unam.mx](mailto:mougel@geociencias.unam.mx)


### Citation:

Mougel, B., Agranier, A., Hemond, C., & Gente, P. (2021). High-resolution isotopic variability across EPR segment 16°N: A chronological interpretation of source composition and ridge-seamount interaction. *Geochemistry, Geophysics, Geosystems*, 22, e2021GC009781. <https://doi.org/10.1029/2021GC009781>

Received 11 MAR 2021

Accepted 13 SEP 2021

## High-Resolution Isotopic Variability Across EPR Segment 16°N: A Chronological Interpretation of Source Composition and Ridge-Seamount Interaction

Berengere Mougel<sup>1</sup> , Arnaud Agranier<sup>2</sup>, Christophe Hemond<sup>2</sup>, and Pascal Gente<sup>2</sup>

<sup>1</sup>Centro de Geociencias, Universidad Nacional Autónoma de México, Querétaro, Mexico, <sup>2</sup>CNRS, IUEM, UMR 6538 Laboratoire Géosciences Océan, Université de Brest, Plouzané, France

**Abstract** A high-resolution sampling profile constituted of 52 basalt samples from across the East Pacific Rise (EPR) was investigated. These samples provide a unique opportunity to study the coeval recording of isotopic signals derived from sub-marine eruptions at a fast spreading ridge over a time interval of ~320 kyrs. Additionally, the study area is marked by the presence of a neighboring seamount chain that has recently caused the ridge to jump twice toward it. Combining previous geochemical studies and bathymetry, we established a first-order chronology between analyzed samples, and have reconstructed the evolution of basalt compositions as the ridge and seamounts advance and finally merge. Our data reveal the existence of two distinct types of isotopic variability within the samples. One that has a low amplitude and frequency and is accounted for by the continuous melting of the ambient mantle, indicating a process with a ~125 kyr periodicity. The other, of higher amplitude, is discontinuous in time, and likely reflects the seamounts source influence on the ridge. Our results support a two-step hotspot-ridge interaction including a first stage (≥600 ka) of regional enrichment of the depleted ridge mantle by hotspot material; and a second, more recent (at least 300 ka) even wherein ambient mantle melts mixed with proximal melts from heterogeneous seamounts sourced nearby. We also propose that the ancient gabbroic component previously identified in this region appeared very recently (<hundreds ya) as erupted lavas are exclusively recorded in a cluster proximal to the axial zone of the ridge.

**Plain Language Summary** The Earth's mantle makes up 80% of the planet's volume; however, mantle rocks are rare at the surface. At mid-ocean ridges, the mantle experiences melting and derived melts may reach the Earth's surface as volcanic basalts. These rocks continuously record the geochemical signature of their mantle source region. Very little is known about the evolution of lava composition over time due to the difficulty of sampling off-ridge axis igneous rocks. This study focuses on a specific portion of the East Pacific Rise at ~16°N, where it interacts with a nearby hotspot. Basaltic rocks were collected with the French submersible Nautile (Ifremer) across the ridge axis during the cruise Parisub (2010, R/V L'Atalante). The sampling profile obtained covers a period of time that allows long term monitoring and assessment of mantle sourced signals and fluctuations in erupted basalts for >300 kyrs. We have established a relative chronology between these samples, and propose a paleo-reconstruction of the area accounting for both the isotopic variations observed and previously reported geophysical results. Our new results also suggest rapid magma transfers within the crust independent of melting of seamounts and/or ridge sources, including periodic injections of enriched mantle material into the ridge-melting region.

## 1. Introduction

Radiogenic isotope compositions of mid-ocean ridge basalts (MORB) have been documented for decades along global ridge axes, and corresponding databases indicate that there are compositional variations along various active spreading centers. However, our understanding of temporal variations in the chemistry of lavas produced on-axis is limited by the restricted number of studies and related data available for off- or across-axis ridges (Niu et al., 1999; Regelous et al., 1999) (excluding seamounts). For example, ridge flanks are typically covered rapidly by sediments, which render them difficult to access. Moreover, distinguishing the ages of MORB lavas collected relatively close to each other remains problematic. Magmatic processes such as partial melting, crystal growth, and fractional crystallization produce disequilibrium between

© 2021 The Authors.

This is an open access article under the terms of the [Creative Commons Attribution-NonCommercial License](https://creativecommons.org/licenses/by-nc/4.0/), which permits use, distribution and reproduction in any medium, provided the original work is properly cited and is not used for commercial purposes.

short-lived Uranium-series nuclides in young lavas (<350 kyrs), and the study of U-series disequilibrium has helped to resolve the time-scales of magmatic processes in different tectonic contexts (e.g., Hemond et al., 1994; Lundstrom, 2003; Peate & Hawkesworth, 2005; Turner et al., 2011; Zou et al., 2002). However, obtaining comprehensive and high quality U-series data on suites of MORB is not straightforward for a several reasons; (a) they have generally lower abundances of incompatible trace elements, (b) they may be affected by seawater alteration and Fe-Mn crust contamination, (c) they have unconstrained eruption ages, which make post-eruption radioactive decay corrections difficult, and (d) the source composition, the rate and type of melting, and melt-mantle interactions can all affect disequilibrium. Together these factors make sample dating analytically and interpretation challenging, and generally model dependent. Although the time scales at which magmatic and source processes under oceanic ridges operate are now better constrained (e.g., Brandl et al., 2016), continuous tracking of these processes over a sufficiently long period of time within eruption records from a single spreading center continues to pose problems due to limited and/or poorly located sampling.

Significant major element variations have been documented in some off-axis dredged samples from northern sections of the EPR, and are believed to reflect changes in the melt supply regime of the axial magma chamber over intervals of 300 kyrs (Batiza et al., 1996; Perfit et al., 1994; Regelous et al., 1999; Reynolds et al., 1992). However, the primary problem with samples derived from dredging is that the precise sample locations and their structural/geological context are uncertain, preventing the establishment of stratigraphic relationships between the samples collected (i.e., distinction between lava flows, and their relative chronology). Recently, volcanic glass hosted in sediments recovered by piston core sampling along the Juan de Fuca ridge now present another promising technique capable of sampling a continuous and high-resolution time sequence of volcanic activity (Ferguson et al., 2017). By combining geochemical and stratigraphic interpretations it is now possible to constrain the temporal and compositional evolution of magmatic melts over time-periods ranging from 10 to 100 kyrs for samples derived from a single core. However, these logs can only account for magma chamber dynamics over relatively short periods of time (e.g., storage, differentiation, extraction, and frequency of recharges etc.). It is unclear yet if distinct cores collected at various distances from a given ridge axis can be successfully compared with one another in order to cover longer time intervals that are more representative of mantle source processes.

Alternatively, the study of isotopic variability in magmatic samples collected across ridge axes permits us to address the time scale at which changes in mantle sources may occur (e.g., Perfit et al., 1994; Gill et al., 2016; Waters et al., 2011). In contrast to major and trace element concentrations, which can be fractionated by magmatic processes, radiogenic isotopes (and in most cases similarly incompatible element ratios) only rely on mantle source compositions and later crustal contamination processes (mostly negligible in oceanic domains). They are therefore the preferred tools for tracing source changes. These isotopic data, combined with incompatible element data and element ratios can be powerful tools for understanding the nature of source magma histories. Based on radiogenic isotope compositions of samples collected by the submersible (Nautile) across the Central Indian Ridge (CIR) at 19°N, Cordier et al. (2010) prove that some isotopically enriched-type basalts were symmetrically distributed on both sides of the CIR. These authors suggest that a compositionally heterogeneous mantle, associated with changes in melt production rates at intervals of about 150–200 kyrs, were responsible for the variations observed. On a larger scale, transform faults also represent a window into the isotopic diversity of both crustal and mantle rocks over millions of years, associated with both mantle source heterogeneities and/or thermal effects (Brunelli et al., 2018; Cipriani et al., 2004; Wendt et al., 1999). Nevertheless, these studies, covering long periods of time, still suffer from wide sampling gaps equivalent to thousands or even hundreds of thousands of years, and therefore likely reflect a truncated view of mantle source evolution. Sampling resolution at mid ocean ridges can indeed lead to a significant bias in the way mantle heterogeneities are interpreted based on mid-ocean ridge seafloor material studies. This is also true for single seamounts, which can show large isotopic variability (e.g., Anderson et al., 2021; Niu et al., 2002). For example, Mougél et al. (2014, 2015) demonstrated that the isotopic variability recorded over a single 10 km portion of an EPR segment, sampled every 200 m, can be equivalent to that of the entire EPR database (~9,000 km), and yet reveal the existence of peculiar mantle source signatures.

This work provides new Sr-Nd-Hf-Pb radiogenic isotope, as well as major and trace element data on 52 basalt samples collected by submersible along a 25 km profile across the present-day EPR at  $\sim 16^{\circ}\text{N}$ , and the traces of its two former parallel axes. These data represent one of the highest-resolution efforts studies to date that investigate the temporal fluctuations in mantle-sourced magmas at a mid-ocean ridge system. Here we provide a unique data set that documents the isotopic responses of the MORB related to the convergence between a fast spreading ridge and a suspected hotspot over the last  $\sim 320$  kyrs. Based on careful interpretation of bathymetric data and regional context of this area, we attempt to address the following two major questions; (a) Is it possible to establish a relative chronology of MORB samples, and in turn develop a continuous interpretation of various isotopic signals as the ridge migrates toward the seamount source and (b) What possible factors have led to the observable isotopic diversity in MORB from this area.

## 2. Geological Context

### 2.1. Tectonic Settings

The study area is located in the northern sector of the EPR where the Pacific and Coco plates diverge at a full spreading rate of  $\sim 85$  mm/y. Between the Rivera and Orozco transform faults, the EPR is divided into three segments (Figure 1a), which have axial morphologies that are drastically different from one another. This study focuses on the southern segment, commonly referred to as the  $16^{\circ}\text{N}$  segment, or North Orozco segment. The segment of study is 115 km long, 400 m shallower and twice wider ( $\sim 10$  km) than the rest of the EPR. On its western side a prominent seamount chain, the “Mudskipper Seamounts” ( $< 0.8$  Ma) intersects with the ridge axis at its widest section (e.g., Bender et al., 1998; Carbotte et al., 1998, 2000; Macdonald et al., 1992; Scheirer & Macdonald, 1995; Weiland & Macdonald, 1996). This area is also marked by the presence of an off-axis magma lens 1.2 km westward of the present axis (Carbotte et al., 2000; Le Saout et al., 2018). The best illustration of the merging between these two magmatic systems is the existence of the recent ( $\sim 3$  ka) “Split Seamount” that has been separated in half by the current axis (Figures 1b and 1c). The unique morphology of this segment has been attributed to a remarkably high magmatic supply due to the presence of a small hotspot to the west of the ridge. Two previously reported parallel steps are visible in the bathymetry on either side of the ridge axis in this area (Figure 1b). In Addition, they are asymmetric with respect to the current axis, with the eastern step being located further away from the ridge’s axis than the western one. They bound a 100–150 m shallower and smoother seafloor region interpreted to be the result of increased magmatic production compared to “normal” ridge conditions along this segment. This uplift event occurred  $\sim 600$  ka according to magnetic data interpretations (Cormier et al., 1998), and the visible asymmetry between the two bathymetrical markers is related to the recent two-stage migration of the rift segment in the direction of the Mudskipper Seamounts in the last 300 kyrs (Carbotte et al., 2000; Le Saout et al., 2014, 2018; Scheirer & Macdonald, 1995; Shah & Buck, 2006; Weiland & Macdonald, 1996). On the larger scale, this segment has evolved over the last 8 Myrs of recorded history of the northern Pacific ocean (Mammerickx & Klitgord, 1982), which started with an eastward ridge jump of several hundred kilometers, and progressively led to the abandonment of the “Mathematician fossil ridge” in favor of the current EPR. In addition, numerous seamounts are located in this area on both sides of the EPR (Figure 1a). To the west, the volcanic structures are attributed to the presence of a small heterogeneous hotspot (i.e., “Mathematician Hotspot”) responsible for the formation of the “Western plateau,” the “Northern Seamounts” and the “Mudskipper Seamounts” (Donnelly, 2002; Langmuir et al., 1998), while the origin of the “Eastern Seamounts” still remains uncertain. Finally, the tectonic and magmatic complexity of this region is also recorded in the geochemical composition of basalts from the  $16^{\circ}\text{N}$  segment, which displays a unique and remarkable isotopic variability (Donnelly, 2002; Mallick et al., 2019; Mougél et al., 2014, 2015).

### 2.2. Geochemical Overview and Local Components

The geochemical composition of the northern EPR MORB is very peculiar, in that its variability coincides with ridge discontinuities (even small offsets) (Figure 2). Third, and higher order offsets are generally considered as reflecting changes in the axial magma chamber, while first and second order offsets are often related to changes in the composition of the mantle. Recently, based on the correlation observed between trace elements and isotopes, Mallick et al. (2019) demonstrated that the mantle source and extent of melting are the main factors that control trace element variability in the northern part of the EPR (rather than crustal

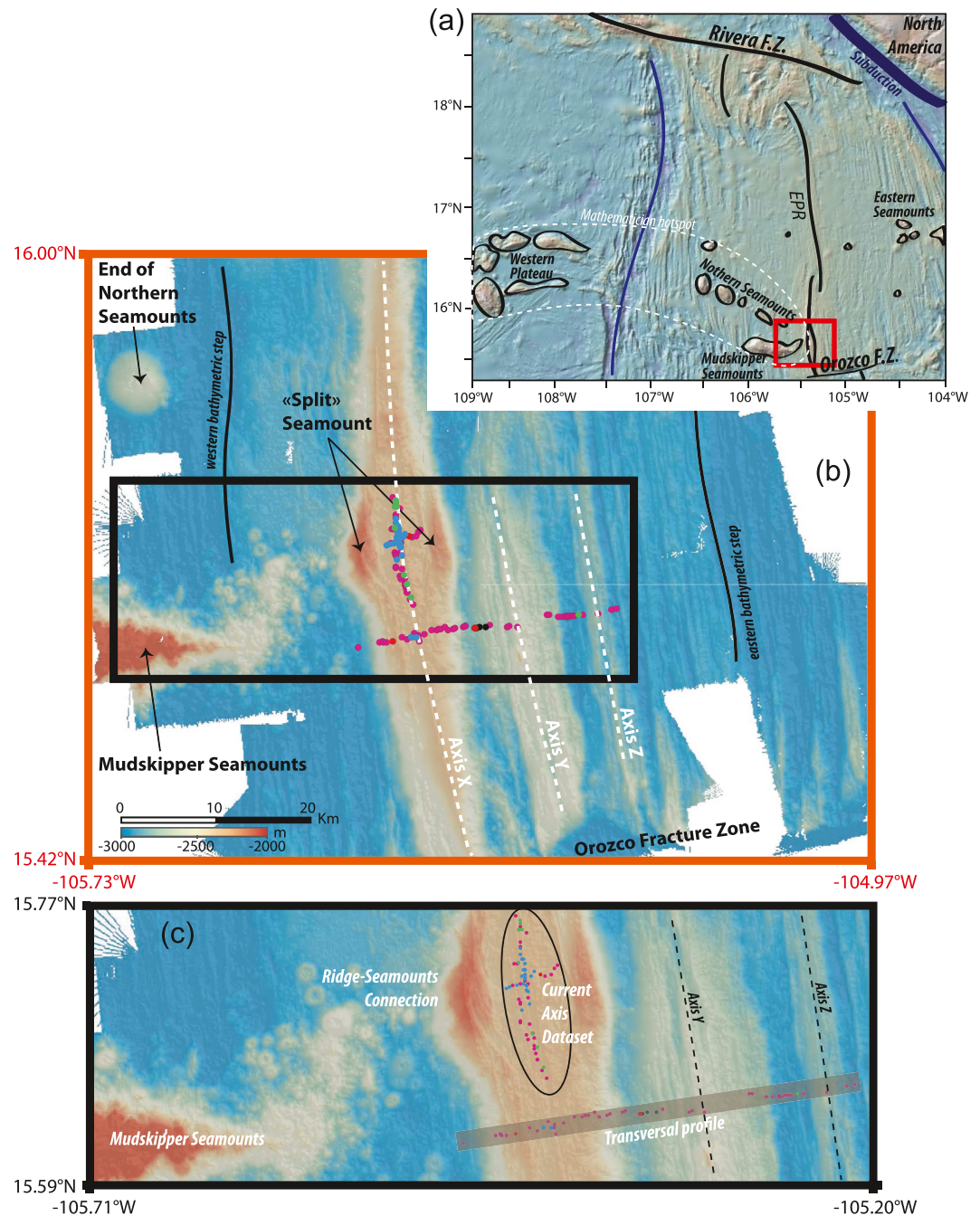


**Figure 1.** Sample locations and bathymetry of the study area. (a) General map presenting the main physiographic features between the Rivera and Orozco Fracture Zones (FZ), and the present study area location (red rectangle). (b) Bathymetry (40 m-grid spacing) of the study area showing the current axis (X) and two relic axes (Y and Z), the “Mudskipper Seamounts” chain, the “Split Seamount” on top of the axis, as well as two high-resolution sampling profiles. Two parallel ridge-steps are visible in the bathymetry on either side of the current axis. They bound a ~100–150 m shallower and smoother seafloor region, and are interpreted as the result of an increase in the magmatic budget of the segment ~600 ka. The color code adopted for all samples refers to their isotopic fingerprints. Pink: Ambient Mantle signature (AM); Blue: Mudskipper-type 1 signature (M1); Green: Mudskipper-type 2 signature (M2); Red: enriched mid-ocean ridge basalts (E-MORB); Black: depleted normal mid-ocean ridge basalt (N-MORB). (c). Focus on the sampled zone. All samples were collected by submersible during the cruise “PARISUB” (2010, R/V L’Atalante). Along current axis data are derived from Mougél et al. (2014). The dark rectangle highlights the transversal profile corresponding to the data presented in this study. It crosscuts all 3 axes. Also of note is the eastward propagation of the Mudskipper Seamounts toward the ridge, and their merging at the center of the segment.

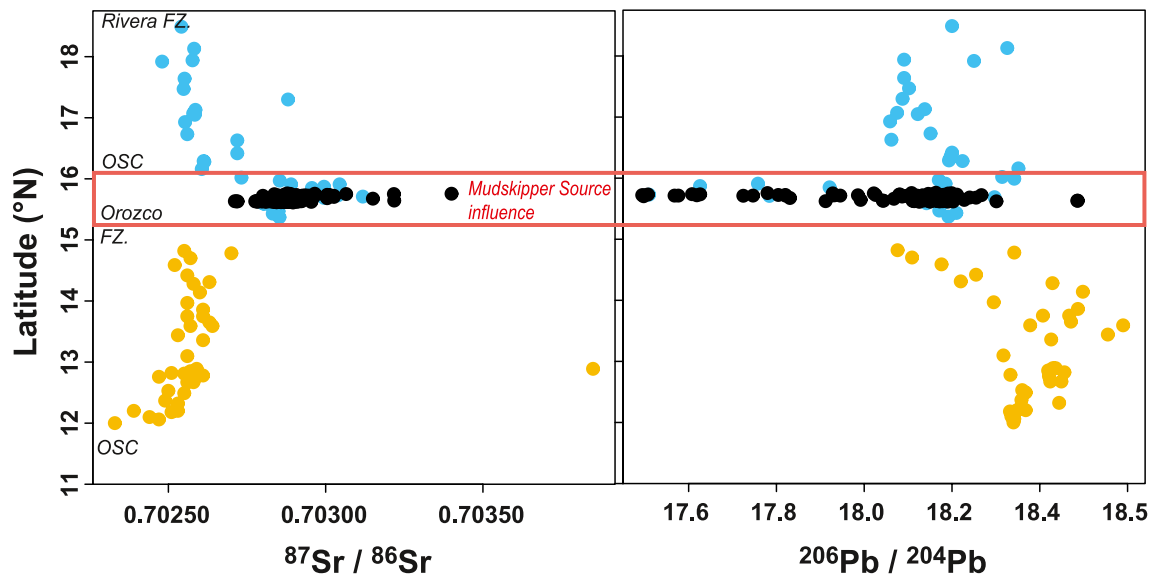


**Figure 2.** Evidence for ridge-hotspot interaction. Latitude versus Sr (left) and Pb (right) isotopic compositions of EPR basalts between the 12°N overlapping spreading center (OSC) and the Rivera F.Z. at 19°N. Black circles correspond to samples from the current study area. Blue circles are data obtained by Donnelly (2002), while orange circles represent data from Castillo et al. (2000). Notably, a peculiar isotopic signature emerges between the Orozco F.Z. and the 16°N OSC due to the interaction with the source of the Mudskipper Seamounts.

processes). In line with the work of Donnelly (2002), and Mougél et al. (2014, 2015), Mallick et al. (2019) confirmed that at least three components are necessary to account for the chemical and isotopic variability of the northern EPR: a depleted mantle, an enriched mantle, and an ancient gabbroic source (converted into pyroxenites). The depleted component is found in the composition of the Eastern Seamounts, while the enriched component is represented in the composition of western off-axis magmatism (i.e., the Western Plateau). Finally, the gabbroic component can be observed in the composition of lavas from the Mudskipper Seamounts, and those from the North Orozco segment, precisely where the Mudskipper Seamounts and the ridge intersect (Figure 1). On-axis basalts from this segment exhibit a wide range of isotopic compositions representative of these three main components (Mougél et al., 2014, 2015). Castillo et al. (2000) noted that at 14°N an isotopic transition takes place, shifting from a depleted to a more enriched mantle signature (Castillo et al., 2000; Donnelly, 2002). This isotopic change is visible in Figure 2, which illustrates the distribution of Sr and Pb isotope compositions of EPR basalts between 12°N (South-Orozco segment) and 19°N (Rivera F.Z.). Of particular interest, between the Orozco fracture zone and the 16°N Overlapping Spreading Center (OSC) the lavas exhibit unique compositions with a wide variability that trends toward more radiogenic Sr, and very unradiogenic Pb (combined with a more unradiogenic Nd and Hf composition). This sharp change has been attributed to the influence of the hotspot on the ridge. This interaction is today manifested by the apparent connection between the Mudskipper Seamounts chain and the ridge axis (Figures 1b and 1c). Acknowledging that the isotopic signatures of the basalts from this area are complex, the dense and high-resolution sampling obtained along the current axis provided by Mougél et al. (2014, 2015), together with our new across-axis data, allow a far more precise characterization of the isotopic variability recorded in MORB of this segment (Figure 3).

In general, isotopic compositions of global oceanic basalts are often described in terms of mixing proportions between “mantle zoo” end-members: HIMU, EM1, EM2, and DMM (Hart et al., 1992). Even though this nomenclature is useful on a global scale to decipher the origin of basalt signatures and to compare them with each other, at a local scale it is not necessarily well suited to the linking of physiographical features observed with basalt compositions. For example, in the case of a hotspot-ridge interaction, at least two distinct mantle sources (being themselves products of former mixtures) are implicitly involved. In order to understand the evolution of this interaction, it is more appropriate to characterize the mixing relationships of these two sources by referring to their local end-members (i.e., the hotspot and the ridge mantle sources),

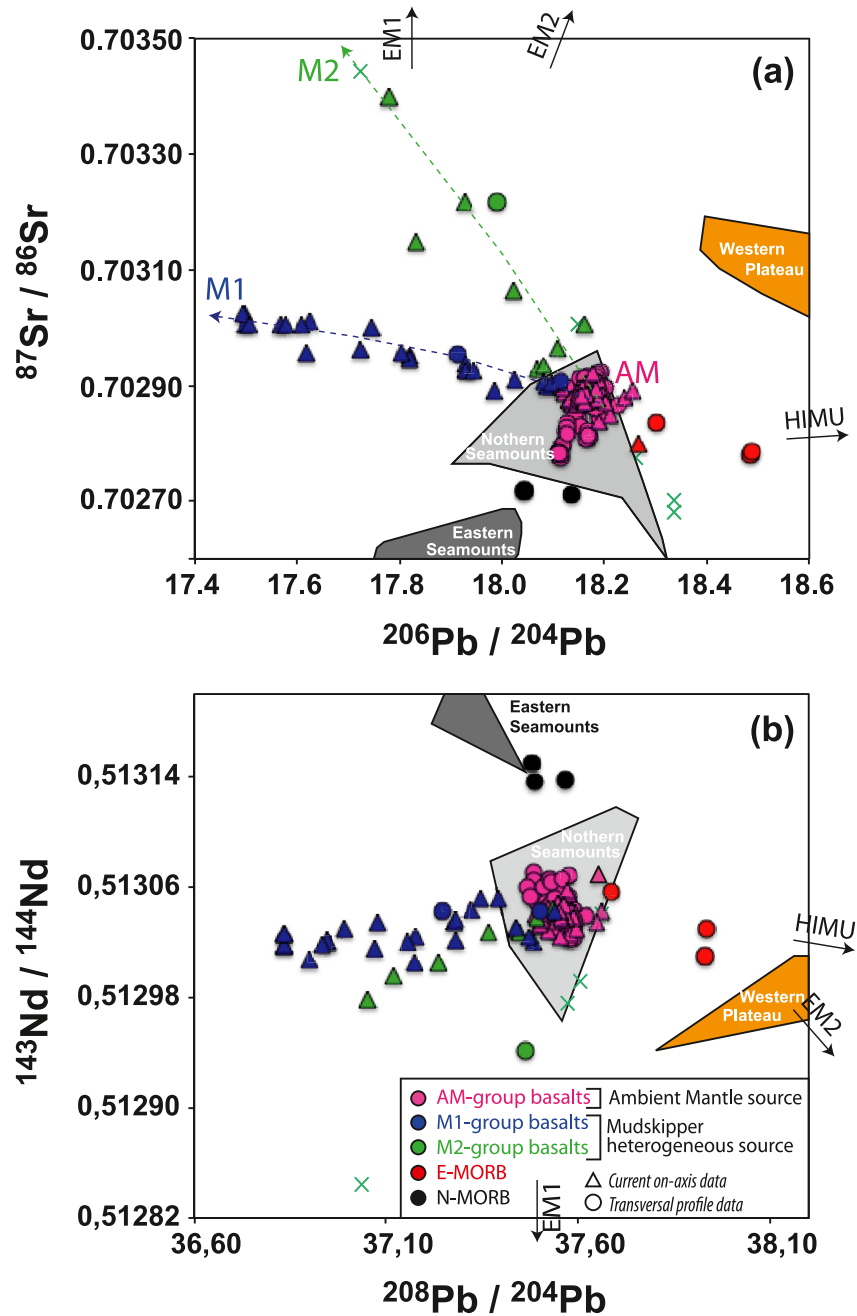


**Figure 3.** Identification of the local endmembers involved in the composition of basalts from the study area. (a) Sr versus Pb isotopic data. Colored fields correspond to the composition of the main off-axis volcanic edifices of the region (see Figure 1a). The composition of the Eastern Seamounts are represented in dark gray, that of the Northern Seamounts alignment in light gray, and that of the Western Plateau in orange (Donnelly, 2002). Green crosses indicate sample data from the Mudskipper Seamounts chain (Donnelly, 2002), triangles correspond to MORB data from the current axial profile (Mougel et al., 2014) and circles indicate samples obtained from the transversal profile (this study). Pink circles represent samples with an Ambient Mantle signature (AM-group), and form a convergent zone in the center of the figure from which the main mixing trends depart. These samples display intermediate compositions between those of the Western Plateau and the Eastern Seamounts, and are similar to the Northern Seamounts alignment in compositions. Blue (M1-group) and green (M2-group) samples are affected by the influence of the Mudskipper Seamounts heterogeneous source on the ridge. They are distributed along two main binary mixing trends between AM-group and the Mudskipper type 1 (M1) or type 2 (M2) components, respectively. Both trends trend toward more unradiogenic Pb and more radiogenic Sr isotopic compositions, although the M2-group has higher  $^{87}\text{Sr}/^{86}\text{Sr}$  ratios for given  $^{206}\text{Pb}/^{204}\text{Pb}$  values. N-MORB samples (black) have intermediate compositions between those of the Eastern Seamounts and the AM-group basalts. E-MORB samples (red) trend toward HIMU. (b) Nd versus Pb isotopes. The distinction between M1 and M2 trends is distinctly less notable in this diagram. Nevertheless samples influenced by the Mudskipper Seamounts source clearly depart from AM group basalts in that they exhibit Pb and Nd compositions comparably less radiogenic.

rather than to the primary mantle end-member compositions, which are irrelevant to the local geological context.

In Figure 3a we present the Sr versus Pb, isotopic composition of samples from our study area for both on- and across-axis data. These data are distributed along two binary (or pseudo binary, Douglass & Schilling, 2000) mixing trends that represent the interplay between the ambient ridge mantle source, and the Mudskipper Seamounts source. These two principle trends form a 3-component system comprised of: The Ambient Mantle (AM, purple symbols), the Mudskipper type-1 component (M1, blue symbols) and the Mudskipper type-2 component (M2, green symbols). The Ambient Mantle signature (AM) is common to all the samples and constitutes a convergent region at the intersection between all mixing trends (Figure 3a), and has intermediate compositions between the Eastern Seamounts (dark gray field) and the Western Plateau (orange field, Figure 3a). When a supplementary component (M1 or M2) is added to the AM component, the composition of the mixture departs from this convergent field following a mixing line in the direction of the other end-member. When examined in Sr-Pb isotopic space, the mixing relationships and the entirety of the isotopic diversity observed in the samples from this area are best revealed, and they display a clear distinction between M1 and M2 signatures (this distinction is less apparent in the other isotopic spaces). The Sr-Pb plot was therefore used to “classify” the samples according to the isotopic trends to which they belong. Although all samples represent unique combinations of two or more of these components, they can still be attributed to different groups, according to their affinity for one of the components listed above. For example, basalts represented in blue and green in the figures reflect the influence of components M1 and M2 respectively, and represent the input of the Mudskipper Seamounts source (Donnelly, 2002; Mougél et al., 2014). Intriguingly these samples capture both depleted and enriched isotopic characteristics: they display unradiogenic Pb isotopes, whereas Sr, Nd, and Hf isotope compositions are characteristic of geochemically enriched material (Mougél et al., 2014). Specifically, the composition of M1-influenced basalts is their highly unradiogenic Pb signatures ( $^{208}\text{Pb}/^{204}\text{Pb} = 36.83$ ,  $^{207}\text{Pb}/^{204}\text{Pb} = 15.46$ , and  $^{206}\text{Pb}/^{204}\text{Pb} = 17.49$ ) associated with more radiogenic Sr, and less radiogenic Nd and Hf isotopic compositions ( $^{87}\text{Sr}/^{86}\text{Sr} = 0.70303$ ,  $^{143}\text{Nd}/^{144}\text{Nd} = 0.51303$ , and  $^{176}\text{Hf}/^{177}\text{Hf} = 0.28302$ ), which is a unique composition among MORB and OIB databases (e.g., Agranier et al., 2005; Meyzen et al., 2007). The recycling of ancient (>2 Ga) sulphide-bearing gabbros has formerly been proposed for the origin of this signature (Mougél et al., 2014). M2-influenced basalts share similar characteristics with M1 basalts, although they have significantly more radiogenic Sr and less radiogenic Nd and Hf signatures for a given Pb composition (Figure 3). Finally, some of the samples consistently plot outside of the AM, M1, and M2 fields: those that have the most radiogenic Pb are enriched MORB (E-MORB, red symbols), while those that have the least radiogenic Sr compositions are depleted MORB (N-MORB, black symbols). This distinction between samples can also be observed via the major and trace element concentrations, as plotted in Figures 4 and 5 (see results and Section 4.2).

### 3. Samples and Methodology

All the samples analyzed in this study are fresh basaltic glasses that were collected by submersible (Nautilus, Ifremer) during the PARISUB cruise (2010, R/V L'Atalante) across the EPR axis (15°40'N) between 105°28'W and 105°13'W (Figures 1c and 6). The advantage of submersible sampling is that it allows precise selection of sample materials on distinct lava flows based on in-situ observations. Additionally, each sample has precise coordinates that are reported in Tables S1–S3.

This transversal profile is peculiar in that it cannot be read as a continuous temporal sequence wherein the further the samples are from the current axis of the ridge (symmetrically), the older they are, and conversely so. Over the last 300 kyrs, two-ridge jumps occurred (Carbotte et al., 2000; Le Saout et al., 2014, 2018; Scheirer & Macdonald, 1995; Shah & Buck, 2006; Weiland & Macdonald, 1996), which resulted in the generation of younger seafloor domains inside older ones. Therefore longitude versus isotopic compositions plots (Figures 6c and 6d) cannot be directly used for temporal interpretation of the data.

#### 3.1. Relative Chronology: Interpretation Strategy

In order to establish a relative chronology among these studied samples both the sampling profile and the geographic boundaries of separate seafloor domains opened by each of the observable axis must be

determined. Based on the topography of the sampling profile presented in this study, as well as lava flow directions, we have been able to group and assign each of the samples with a respective axis identification that we have termed  $X$ ,  $Y$ , or  $Z$  (Figures 6a and 6b). If we consider  $X$ -axis as representing the current active axis,  $Y$ -axis as representing the trace of the preceding extinct axis, and  $Z$ -axis as representing the trace of the oldest extinct axis, thus all samples belonging to the seafloor domain opened by  $X$ -axis are therefore younger than those belonging to the domain opened by the  $Y$ -axis, and ultimately those belonging to the domain opened by the  $Z$ -axis. This primary division between samples is the basis for our first order chronology.

At fast spreading centers, melt flux to the axis is high and accretion develops relatively symmetrically compared to slow-spreading oceanic ridges (e.g., Müller et al., 2008). In our study area it has verified via the symmetrical separation of the “split” seamount over the last 3 kyrs, as well as repeated evidence of symmetric lava flow morphology and divergent fronts observed at the Axial Summit Troughs of the 16°N segment (Le Saout, 2015; Le Saout et al., 2014). As a result, we can infer that two samples located equidistant to the same ridge axis should have roughly similar ages. By comparing the angular distance ( $D$ ) to the ridge axis ( $x_i, y_i, z_i$ ) for each sample obtained from the same domain it is possible to determine a relative chronological order for sample emplacement (Figure 7). Two symmetrical half-domains can be assigned to each axis with the most extended side representing the longest time-interval of accretion (i.e., half-domains do not necessarily have the same dimensions due to ridge jump truncations). This longest time-interval of accretion corresponds to a maximum angular distance to the axis  $D_{1/2}$  ( $X, Y, Z$ ) within which all the samples produced by their corresponding axis are included (irrespective of the half-domain to which they belong). In this case the assumption is that we consider symmetric accretion so the  $Dx_i, y_i, z_i$  ( $>0$ ) from both sides of the corresponding axis can be projected on the same  $D_{1/2}$  (Figure 7a)

For each axis ( $X, Y$ , and  $Z$  respectively),  $D_{1/2}X = Dx_0$  ( $x_0 = 19\text{PUB10-03}$ ; the first sample of the profile and the farthest from  $X$ -axis),  $D_{1/2}Y = D_{Y/Z}$  ( $X/Y$ : the location of the boundary between  $Y$  and  $Z$ -type seafloor domains), and  $D_{1/2}Z = Dz_n$  ( $z_n = 10\text{PUB02-02}$ ; the last sample of the profile and the farthest from  $Z$ -axis). It is important to note at this juncture that the primary goal of this study is not to establish a precise chronology, but rather to create a first order chronological profile on a single figure that includes the composition of erupted basalts as the ridge migrated closer to the Mudskipper Seamounts (Figure 7b). Indeed, at very small, to local spatial scales the  $D$  comparison does not guarantee a reliable chronology since lava flows can spread over hundreds of meters to kilometers (Soule et al., 2005) depending on the effusion rate, the magma viscosity and the seafloor bathymetry. Nevertheless, the careful evaluation of lava flow morphologies in the current axial sector, for which high-resolution bathymetric data (1 m in resolution) are available, enables us to determine what the degree of uncertainty is for the  $D$  value. Specifically, the magmatism observed in the study area is primarily dominated by sheet and pillow basalt lava flows (Le Saout et al., 2014), as well as commonly occurring collapsed lava lakes and inflation lava flows. Based on the characterization of the eruptive activity and morphology of the lava flows in this region Le Saout (2015) determined that between 15°37'N and 15°40'N latitude lava flows on average extend over distances  $\leq 500$  m, and only in rare occasions reached distances of 1–2 km (Le Saout, 2015; Le Saout et al., 2014). This maximum distance have been converted into a  $D$  value and the error-bars reported in Figure 7, which in turn constitute the uncertainty of the estimated chronology for samples located close to each other. Finally, off-axis eruptions can also occur (e.g., Sims et al., 2003; Soule et al., 2005), and although this eventuality cannot be entirely ruled out, no eruption of this nature has been identified along the sampling profile based on the careful examination of medium-resolution (40 m) bathymetric data and submersible dive videos (Le Saout, 2015).

Finally, in order to represent the isotopic composition of each sample as a function of the reconstructed chronology, linearization of the  $D$  values of the samples was required to ensure that samples with the same  $D$  value, but origin attributed to different axes cannot be confused. Thus, each sample was defined according to a cumulative angular distance  $D_C(x_i, y_i, z_i)$ , being nothing less than the  $Dx_i, y_i, z_i$  of the sample, to which the corresponding  $D_{1/2}(X)$  values for  $y_i$  samples and the sum of  $D_{1/2}(X)$  and  $D_{1/2}(Y)$  for  $z_i$  samples were added (additional details are provided in the caption for Figure 7).



### 3.2. Analytical Techniques

Analytical protocols used were strictly based on those described by Mougél et al. (2014), in which the authors refer to additional protocols that have been extensively and successfully applied for several decades. Volcanic glass chips were carefully handpicked under a binocular microscope and successively cleaned ultrasonically in both ultra-pure water and ethanol. Following digestion, major and trace element concentrations were obtained via an ICP-AES Jovin Yvon Ultima 2 and Thermo Element2 HR-ICP-MS, respectively at the University of Brest, Pôle Spectrométrie Océan (PSO) following the protocols described in Cotten et al. (1995) and Li and Lee (2006). Isotopic compositions were obtained from a single HF-HNO<sub>3</sub> (3:1) dissolution (after HCl leaching) of 500–750 mg of sample material following the protocols described in Blichert-Toft et al. (2005) for Hf, Nd, and Pb. Sr was separated from the Nd-fraction using Eichrom Sr-specific resin as described in Moynier et al. (2010), and Sr isotopic compositions were analyzed using a Thermo Triton TIMS at the PSO, whereas Hf, Nd, and Pb isotope compositions were analyzed on a Thermo Neptune MC-ICP-MS located at Ifremer-Brest, PSO. Mass bias fractionation was corrected using exponential mass fractionation laws and the following values for Pb, Sr, Nd, and Hf respectively:  $^{205}\text{Tl}/^{203}\text{Tl} = 2.388$ ;  $^{88}\text{Sr}/^{86}\text{Sr} = 8.375202$ ;  $^{146}\text{Nd}/^{144}\text{Nd} = 0.7219$ ; and  $^{179}\text{Hf}/^{177}\text{Hf} = 0.7325$ . Measured values were compared with international standards globally used for standard bracketing: NIST981:  $^{208}\text{Pb}/^{204}\text{Pb} = 36.7007$ ,  $^{207}\text{Pb}/^{204}\text{Pb} = 15.4891$ ,  $^{206}\text{Pb}/^{204}\text{Pb} = 16.9656$ ; JMC475:  $^{176}\text{Hf}/^{177}\text{Hf} = 0.282157$ ; LAJOLLA:  $^{143}\text{Nd}/^{144}\text{Nd} = 0.511858$  and JNDI:  $^{143}\text{Nd}/^{144}\text{Nd} = 0.512115$ ; and NBS987:  $^{86}\text{Sr}/^{87}\text{Sr} = 0.710248$ . Accuracy and precision were verified by repeated measurement of these standards during the period of analysis. The standard values obtained were as follows: NBS987 ( $n = 10$ ):  $^{86}\text{Sr}/^{87}\text{Sr} = 0.710263 \pm 16$  (2sd); JNDI ( $n = 27$ ):  $^{143}\text{Nd}/^{144}\text{Nd} = 0.512076 \pm 32$  (2sd); LAJOLLA ( $n = 11$ ):  $^{143}\text{Nd}/^{144}\text{Nd} = 0.511857 \pm 18$  (2sd); NIST981 ( $n = 23$ ):  $^{208}\text{Pb}/^{204}\text{Pb} = 36.6652 \pm 250$  (2sd),  $^{207}\text{Pb}/^{204}\text{Pb} = 15.4810 \pm 96$  (2sd),  $^{206}\text{Pb}/^{204}\text{Pb} = 16.9283 \pm 86$  (2sd); JMC475 ( $n = 26$ ):  $^{176}\text{Hf}/^{177}\text{Hf} = 0.282148 \pm 16$  (2sd). Sample blanks recorded insignificant amounts contamination for each element when compared to the total amount of each element isolated from sample material.

## 4. Results

### 4.1. Morphotectonic Considerations

The transversal sampling profile examined in this study crosscuts the currently active axis as well as the two previous axes (Figure 6a). Figure 6b illustrates both the bathymetry of the profile and the recorded location for each of the samples. Sample depths ranged from  $-3,000$  to  $-2,300$  m, and longitudes between  $-105.47^\circ\text{W}$  and  $-105.22^\circ\text{W}$ . Three domal structures were identified, each of which increases in size from east to west. They correspond to the traces of the past and current ridge axial zones (Carbotte et al., 2000; Le Saout et al., 2018; Shah & Buck, 2006; Weiland & Macdonald, 1996), which have evolved toward wider and flatter morphologies, being consistent with the increase of the magmatic supply as the ridge approaches the Mudskipper Seamounts chain. This bathymetric profile is significantly different from that of the abyssal hills located to the east and southwest of the sampling profile (Figure 1b). Abyssal hills repeat at higher frequencies than the domes and display lower amplitude depth variations. Observable domes are separated by valleys, for which the deepest point corresponds to the border between seafloor domains belonging to the distinct axes (X: orange; Y: yellow; Z: white, Figures 6b–6d). To the west of Dome X, east of Dome Z, and between Domes Y and Z, the seafloor converges at the same minimum depth of  $-3,000$  m. However, between domes X and Y the lowest point is  $\sim 200$  m shallower. This observation indicates that the X and Y domains are in direct contact, without any Z-type crust interposed between the X and Y-axes. This observation is consistent with a small and recent ridge jump as suggested by Carbotte et al. (2000). In the interval between Y and Z domes the depth profile is more chaotic, however, the boundary between these domes can still be determined precisely due to the orientation and dip of faults and lava flows using the 40 m-resolution map. Based on these observations combined, all samples were systematically grouped according to the axis to which they primarily belong. In addition, the geochemical fingerprint of each sample (as identified in Figure 3) is reported in all other figures for clarity. Statistically, samples from the AM group are much more numerous than those from other basalt groups (AM > M1 > M2 > E/N-MORB) in both the current axial and transversal datasets. As previously mentioned, the seafloor in the study area comprises several distinct types of lava flows: pillow, sheet, and more rarely, inflated lava flows (Le Saout et al., 2014). Therefore it is a worthwhile endeavor to investigate whether the morphology of the lavas flows was somehow related to the geochemical source signature of the samples. Following this line of thought, we combined micro-ba-

thymetric observational data (1 m resolution; Le Saout, 2015; Le Saout et al., 2014) with the precise coordinates of the ~120 samples collected by submersible along the current axial ridge (Mougel et al., 2014). This comparison revealed the absence of link between the type of lava flow and the identified basaltic groups. For example, AM-axial basalts are divided between 50% pillow lavas, 47% sheet flows, and 3% inflation lava flows; while M1-axial basalts are divided between 37% pillow lavas; 63% sheet flows; 0% inflation lava flows, and M2-axial lavas are divided between 25%; 75%; and 0% respectively. Additionally, the size of lava flows observed in our study area varies considerably, but is independent of the type of lava flow (>90% of the flows studied have a maximum length that falls between 100 and 1,000 m).

#### 4.2. Geochemical Variations Along the Sampling Profile and Comparison With Current-Axis Data

This study provides new data from a transversal profile crosscutting the North Orozco segment at its center (Figure 1c). As illustrated in Figures 2–7, our data has been presented together with MORB data obtained from the current along-axis profile collected during the same cruise, and represented with a color code according to the mantle components that best describe them. Figure 3 demonstrates that our new data are in agreement with the data and mantle components as identified by Mougel et al. (2014), and in addition they also confirm the remarkable heterogeneity of the mantle underlying this region. Although these results concur with the axial data set (Figure 3) they also show some specificity. Specifically, major and trace element compositions are generally more homogenous, while the AM signature extends toward more depleted isotope compositions with lower  $^{87}\text{Sr}/^{86}\text{Sr}$  and higher  $^{143}\text{Nd}/^{144}\text{Nd}$  compared to the axial profile, gradually trending toward the compositions reported for samples from the Eastern Seamounts (Figure 3), and from the adjacent EPR segment in the north (Donnelly, 2002, Figure 2). This sampling transect has also been found to record typical N-MORB compositions that have not been detected along the current axis.

The majority of samples from this study are generally slightly fractionated tholeiites with a composition of ~6.2–9.3 wt% MgO (mainly ~7.5 wt%). Only one sample obtained (10PUB02-07) is highly evolved, with 3.2 wt% MgO, and is associated with the highest trace element concentrations observed (Figure 4). Similar MgO content of 8 wt% is observed in M1 and M2-type basalts that also contain higher  $\text{SiO}_2$ ,  $\text{Na}_2\text{O}$ ,  $\text{Al}_2\text{O}_3$  concentrations, but lower CaO, MnO,  $\text{K}_2\text{O}$  than typical AM type basalts. The differences in these samples cannot be attributed simply to fractional crystallization process, but rather suggest a mantle source difference in lithology. Furthermore, some typical E-MORB compositions have also been identified by their major oxide content which displays higher  $\text{TiO}_2$ ,  $\text{Al}_2\text{O}_3$ ,  $\text{K}_2\text{O}$ , and  $\text{Na}_2\text{O}$  concentrations than the other samples, causing them to depart from the general trend of AM-type basalts.

Four distinct types of MORB have now been distinguished (Figure 4): E-MORB, depleted N-MORB, transitional T-MORB, and atypical depleted MORB. Importantly, the delineation between each type coincides with distinctions made based on each samples isotope composition (see Section 2.1.). Most of the samples are T-MORB that possess almost flat REE patterns ( $[\text{La}/\text{Sm}]_{\text{N}} \sim 0.95 \pm 0.05$ ; Figure 5) and a negative Eu anomaly, when normalized to the Primitive Mantle. They are representative of AM-group melts and are more enriched ( $0.13 \leq \text{K}_2\text{O}/\text{TiO}_2 \leq 0.21$ ) than the depleted N-MORB samples ( $[\text{La}/\text{Sm}]_{\text{N}} = 0.5$ ;  $\text{K}_2\text{O}/\text{TiO}_2 = 0.06$ ) but less enriched than the E-MORB ( $[\text{La}/\text{Sm}]_{\text{N}} \sim 1.5$ ;  $\text{K}_2\text{O}/\text{TiO}_2 = 0.34$ ). Samples belonging to M1 and M2 isotopic trends have intermediate trace element compositions between the T-MORB and the atypical depleted MORB. In general, these samples display depletion in both the lightest and the heaviest rare earth elements (LREE and HREE, respectively), positive Eu, Sr, and Ba anomalies, as well as negative Th, U, and Pb anomalies.

Nd and Pb isotope compositions versus the longitude where samples were obtained are presented in Figures 6c and 6d where it is demonstrated that Pb isotopes are the most sensitive geochemical tracer that is capable of distinguishing between the different mantle components involved. M1 and M2-type basalts as well as E-MORB can unambiguously be distinguished from the AM signal, however it is not true for N-MORB. Conversely, Nd, Hf and Sr are more sensitive to internal AM isotopic variations (Figures 6c and 7) and can better distinguish between N-MORB from AM-type basalts. Finally, the data obtained in this study all indicate that the AM-signature has been recorded continuously in lavas emitted by all of the three axes

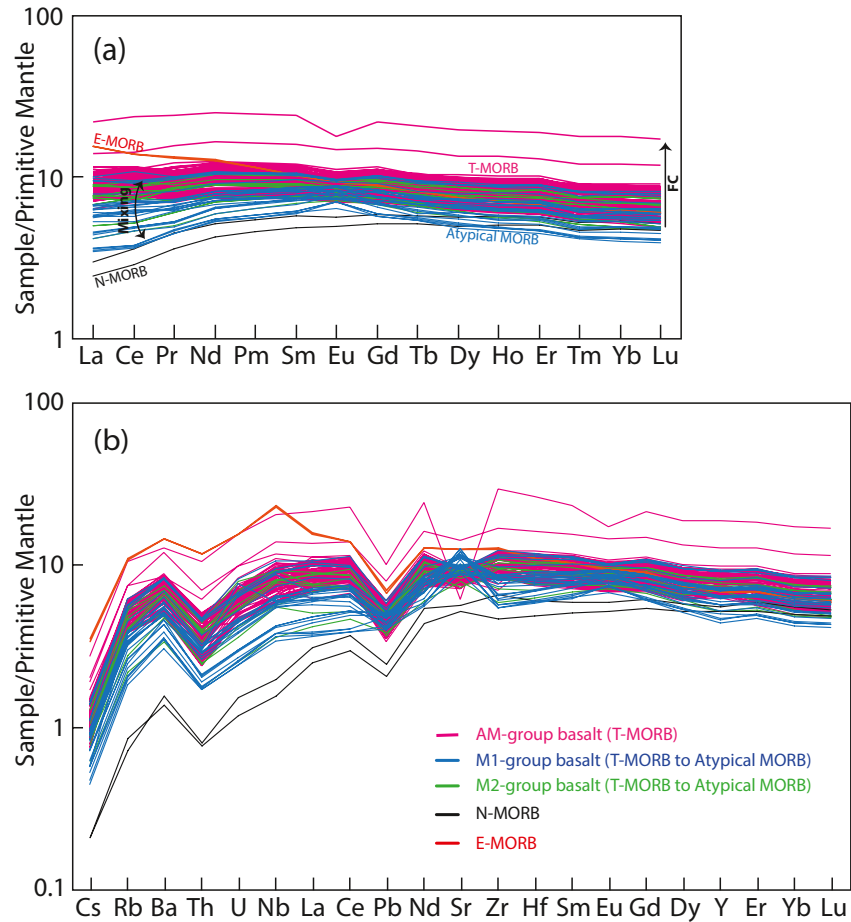


**Figure 4.** Incompatible Trace Element Compositions. (a) Rare Earth Element (REE) diagram and (b) extended trace element diagram normalized to the Primitive Mantle composition (McDonough & Sun, 1995). Four types of MORB can be identified based on these diagrams. Most of the samples are T-MORB and belong to the AM group and exhibit relatively homogeneous compositions, although two samples show clear evidence for fractional crystallization. M1 and M2-group samples display compositions that are intermediate between T-MORB and depleted atypical MORB (the latter having a slight depletion in both LREE and HREE) reflecting binary mixing. E-MORB and N-MORB samples are also present. See Figure 3 for sample color-coding.

(X, Y, Z), while M1 is restricted to the X-axis, M2 to the Z and X-axes intervals, and N-MORB to the Y-axis domain only, while the E-MORB are found in both the X and Y-axis domains.

## 5. Discussion

### 5.1. First Order Chronological Interpretation

Distance and time of seafloor emplacement at mid ocean ridges are linked by the spreading rate, which is presently reaching 85 mm/year along this segment of EPR. Our analysis has allowed the delimitation of the seafloor domains related to each axis (see Section 4.1) as well as their maximum half lengths  $D_{1/2}$  (X, Y, Z) (see Section 3.1) allowing us to test if they are consistent with the current spreading rate, as well as the time constrains provided by geophysical data. Considering the total length of the sampling profile (25 km), a half-spreading rate of 42.5 mm/a, and by converting  $D_{1/2}$  (X, Y, Z) values into kilometers, we can estimate that the  $D_{1/2}X$ ,  $D_{1/2}Y$ , and  $D_{1/2}Z$  domains should be equivalent to periods of time that are approximately 140, 130, and 50 kyrs, respectively. This is consistent with previous geophysical reconstructions that suggest two ridge-jumps in the last 300 kyrs (Carbotte et al., 2000; Shah & Buck, 2006). Thus, by summing these time-intervals we can constrain that our results reasonably document geochemical variability over the last

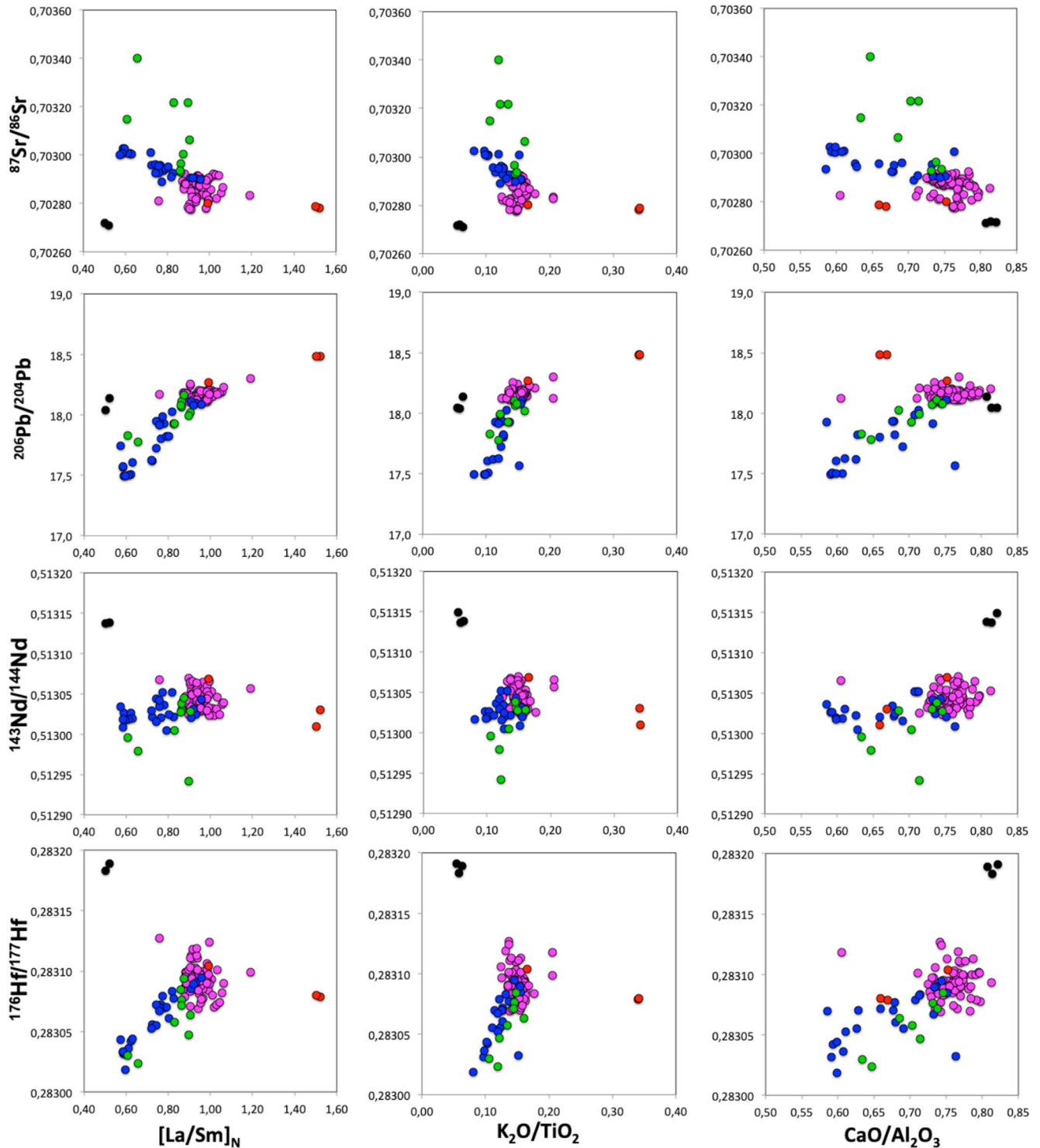


**Figure 5.** Source versus Magmatic Processes. Left Panel: Sr, Nd, Pb, and Hf isotopes versus  $[\text{La}/\text{Sm}]_N$ . Middle Panel: Sr, Nd, Pb, and Hf isotopes versus  $\text{K}_2\text{O}/\text{TiO}_2$ . Right Panel: Sr, Nd, Pb, and Hf isotopes versus  $\text{CaO}/\text{Al}_2\text{O}_3$ . All data from the axial and transversal profiles are here represented together. The strong co-dependence between major/trace elements and isotopic composition suggests that mantle heterogeneity and mixing effects mainly control the composition of the lavas in this area rather than partial melting and/or fractional crystallization processes. See Figure 3 for sample color-coding.

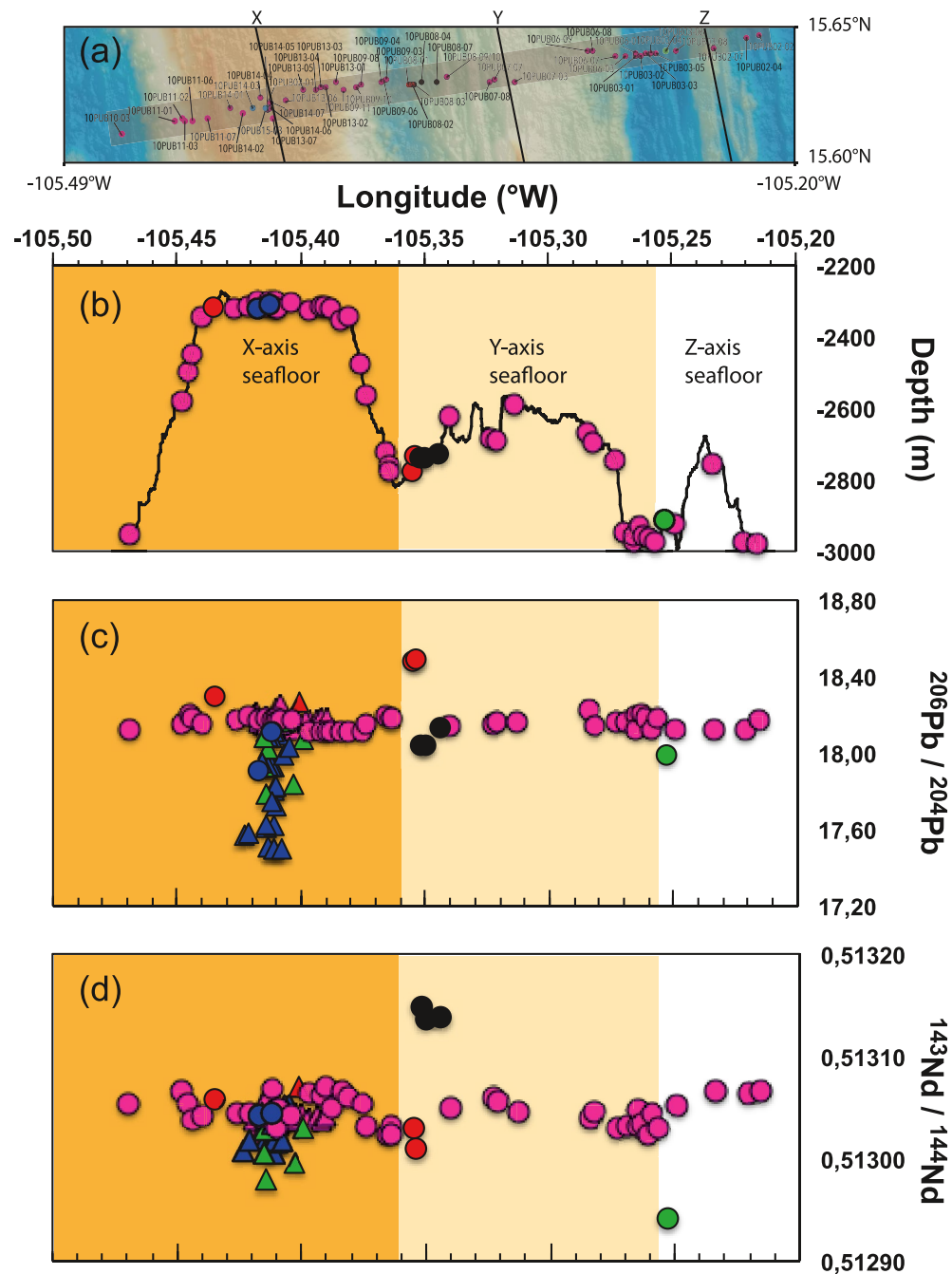


**Figure 6.** Samples location, bathymetric profile and isotopic compositions. (a) Samples location along of the transversal profile. (b) Depth versus Longitude showing the bathymetric profile of the sampling transect, and the boundaries between the seafloor domains created by the opening of the present axis X (orange), the relic axes Y (yellow), and Z (white). Sample locations are reported on the profile. (c) Comparison of Pb isotopes versus Longitude. (d) Nd isotopes versus Longitude. See Figure 3 for sample color-coding.

320 kyrs. The close agreement between spreading rate and spatial distribution of seafloor domains along the sampling profile thus provides a first order time-scale of isotopic fluctuations as observed in Figure 7. This figure presents the chronological reconstruction of the isotopic signal recorded successively on the X, Y, and Z-axes. It is akin to a local time-line where both the temporal variations of mantle sources, as well as

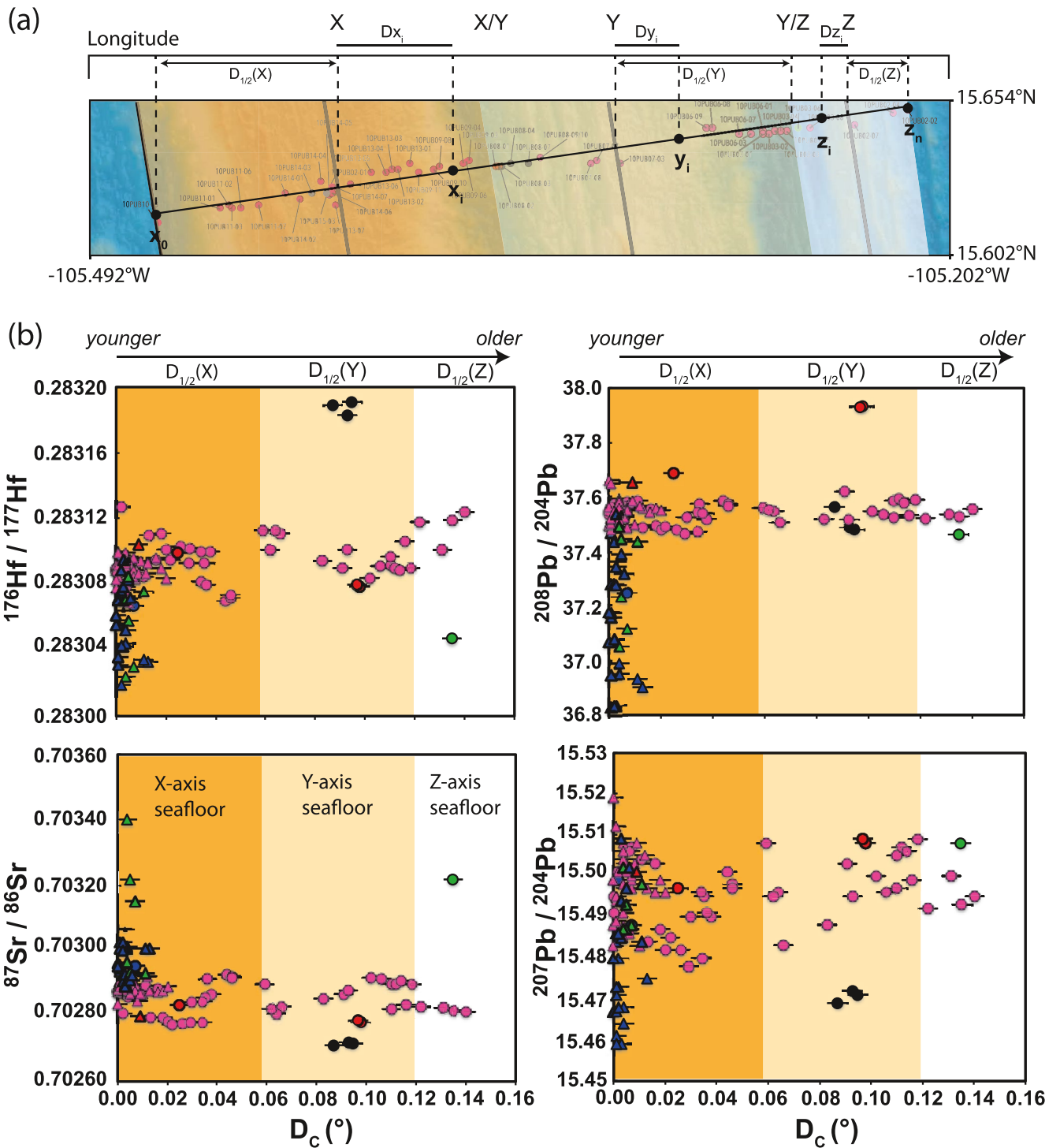
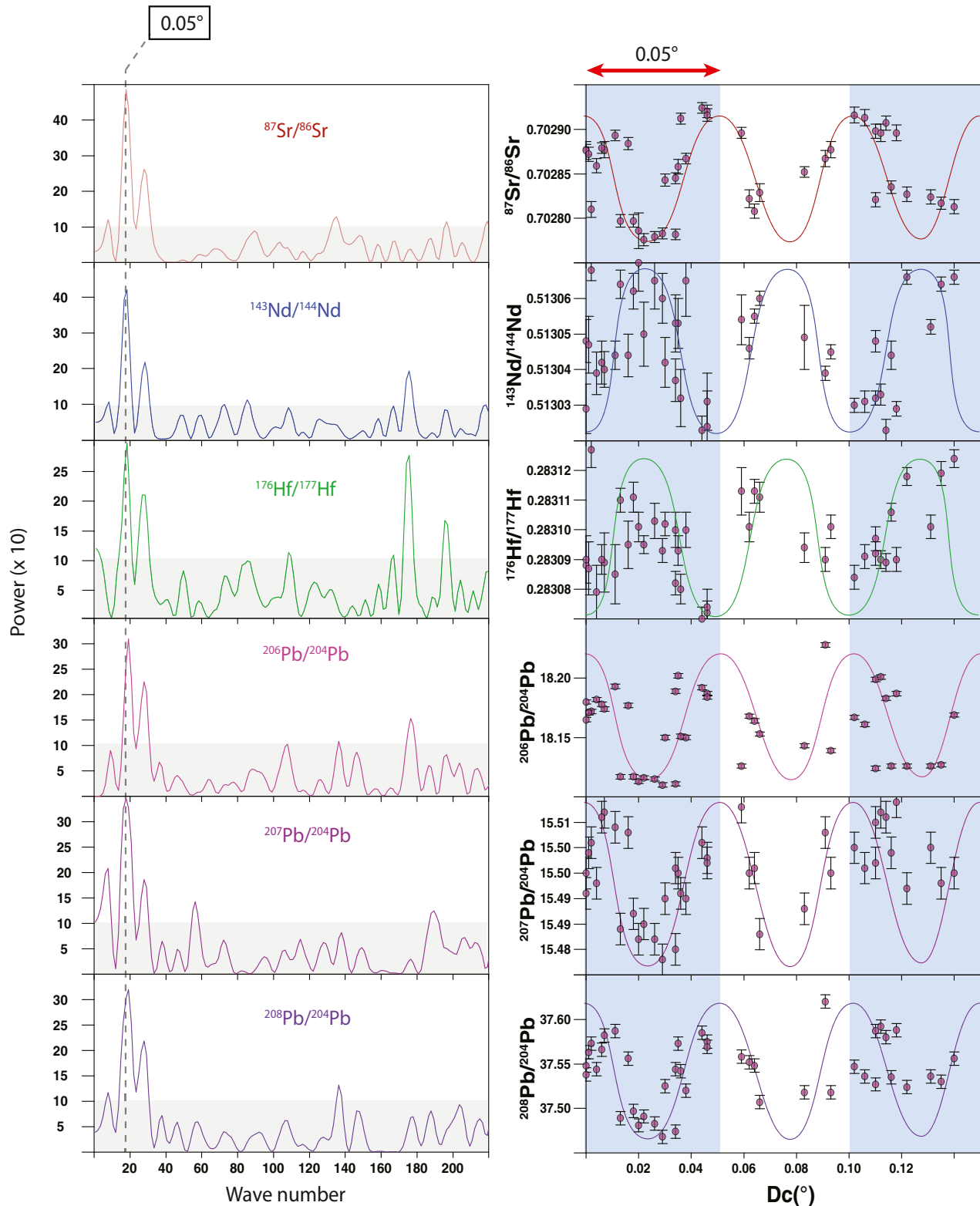


Figure 7.

the impact of the progressive convergence between the ridge and the seamount chain on the geochemistry can be studied. Based on this figure it can be interpreted that:

1. The presence of the M2 signature at the time the Z-axis was active suggests that the source of the Mudskipper Seamounts was already interacting with the North Orozco segment prior to the ridge jumps that occurred (>300 ka). It can also be observed that the amplitude of the first M2 isotopic spike is not small, but in fact falls within the range of M2 values recorded along the current axial profile. As a result it is not possible to infer whether or not the contribution of the Mudskipper Seamounts source may have intensified during the convergence of the two systems based on the geochemistry only. However, geophysical data (Carbotte et al., 2000; Le Saout et al., 2014; Shah & Buck, 2006) suggest that the EPR became more and more inflated while approaching the seamounts, suggesting a progressive increase in the magmatic supply.
2. Samples exhibiting the M1 signature form a dense cluster, specifically, at the connection between the seamounts and the ridge. These signals are also found further south on the transversal profile, but again appear to be restricted to the most axial region of the current axis (Figure 1b). The limitation of the M1-type basalts to the current axis likely implies that the M1 signature is recent; this would be consistent with paleo-intensity measurements from on-axis basalts described by Carlot et al., (2004). The authors were able to identify very young lava flows <100 years at the center of the segment, consistent with the locations where M1-like basalts and the freshest glass samples were collected.
3. The AM signature is continuously recorded along the profile, thus confirming that it is most likely representative of the ambient mantle component, being that it is ubiquitous in all samples. Interestingly, the composition of the AM-type basalts varies over time following an apparently sinusoidal curve suggestive of a cyclic process (Figure 8). The amplitude of this curve does not appear to be affected by the transition from Z to Y, or Y to X domains, indicating that despite ridge jumps, the EPR continuously sampled the same mixed mantle source. However, the observable fluctuations in the AM signal indicate that some mantle heterogeneities have persisted in the ambient mantle lithology resulting in changes over time in the mixing proportions between enriched and depleted materials. The periodicity of the AM signal is further discussed in Section 5.2.
4. Detection of typical N-MORB erupted during the active phase of the Y-axis (with depleted isotopic compositions similar to that of lavas from the adjacent segment located to the north of the study area, as well as the Eastern Seamounts), confirms the mixed nature of the ambient mantle below this segment. Here, AM isotopic signal variations reflect the melting-induced mixing of a 2-component (at minimum) source comprised of enriched (i.e., hotspot) and depleted (i.e., Depleted MORB mantle) materials. Considering the fact that the oldest axis (Z) was already erupting AM-type basalts, we can infer that the evolution from a typical depleted source to a more enriched mixed ambient mantle source must be older than the entire sampling profile. It can be speculated that such modification of the composition of the mantle would have caused significant and lasting changes in the morphology of the segment prior to the development of the Z-axis. The reported evidence of synchronous steps (600 ka) observed in the bathymetry on both side of the current ridge axis (see Section 2.1.) consisting of ~100–150 m uplift of the seafloor in this region (Cormier et al., 1998) may witness a compositional change in the ridge mantle source. Although we do not have corresponding samples that can confirm this interpretation, we believe that this change in the seafloor morphology could correspond to the transition from a depleted- to AM-type mantle below this EPR segment, and marks the beginning of the hotspot-ridge interaction.

**Figure 7.** Chronological interpretation of isotopic compositions. (a) Illustration of the approach used to establish a relative chronology within the transversal sampling profile.  $D_{1/2}(X, Y, Z)$  values represent the maximum angular distance produced by each axis X, Y, Z along the transversal sampling profile.  $x_i, y_i$  and  $z_i$  designate the samples belonging to the domains created by axes X, Y, Z, respectively.  $Dx_i, y_i, z_i$  refer to the angular distance between a sample and its corresponding axis.  $DCx_i, DCy_i, DCz_i$  values represent the cumulative angular distance (for linear graphic representation purposes).  $z_n$  and  $x_0$  correspond to the most distant samples from the oldest (Z) and current (X) axes, respectively. Y/Z: is the apparent geographical limit between the Y and Z domains. Long(): is the longitude of indicated features if in decimal format. The parameters listed above were calculated as follows:  $D1/2(X) = |\text{Long}(X) - \text{Long}(x_0)|$ ;  $D1/2(Y) = |\text{Long}(Y) - \text{Long}(Y/Z)|$ ;  $D1/2(Z) = |\text{Long}(Z) - \text{Long}(z_n)|$ ;  $Dx_i = |\text{Long}(X) - \text{Long}(x_i)|$ ;  $Dy_i = |\text{Long}(Y) - \text{Long}(y_i)|$ ;  $Dz_i = |\text{Long}(Z) - \text{Long}(z_i)|$ ;  $DCx_i = Dx_i$ ;  $DCy_i = D1/2(X) + Dy_i$ ;  $DCz_i = D1/2(X) + D1/2(Y) + Dz_i$ . N.B. Here the assumption is made that Z and  $\Sigma z_i$  are older than Y and  $\Sigma y_i$ , which are in turn older than X and  $\Sigma x_i$ . (b) Hf, Sr, and Pb isotopes versus Cumulative angular distance  $D_c$  (°). The figure should be read as follows: from left to right, the higher the  $D_c$  value, the older the seafloor is. Orange, yellow, and white fields correspond to the seafloor domains opened by the X, Y, and Z axes, respectively. Symbols and colors of all samples are the same as presented in other figures. The horizontal error bars correspond to the uncertainty of  $D$  values related to the average spreading length of lavas estimated in the study area (see methodology and discussion). Note that the variations in AM-basalts signal (pink) are of relatively low amplitude but repeat in a cyclical way, on the contrary, M1 and M2-type basalts (blue and green) show higher amplitude and more episodic variability. See discussion for more details.



**Figure 8.** Periodicity in the AM signal. Left panel: Lomb and Scargle periodograms of Sr, Nd, Pb, and Hf isotopes. The horizontal scale represents the wavenumber (the reciprocal of the wavelength) in  $^{\circ-1}$ , while the vertical scale represents the dimensionless power spectrum (square of the standard-deviation-normalized amplitudes). Significant peaks ( $P > 1$ ) indicate that sine functions with wavelengths of  $0.05\text{--}0.035^{\circ}$  adequately fit the spectrum of the observed AM isotopic variations. Right Panel: spectra of isotopic variations along the cross-section. A sine function of  $T = 0.05^{\circ}$  is represented in order to visually highlight the effectiveness of the periodograms.



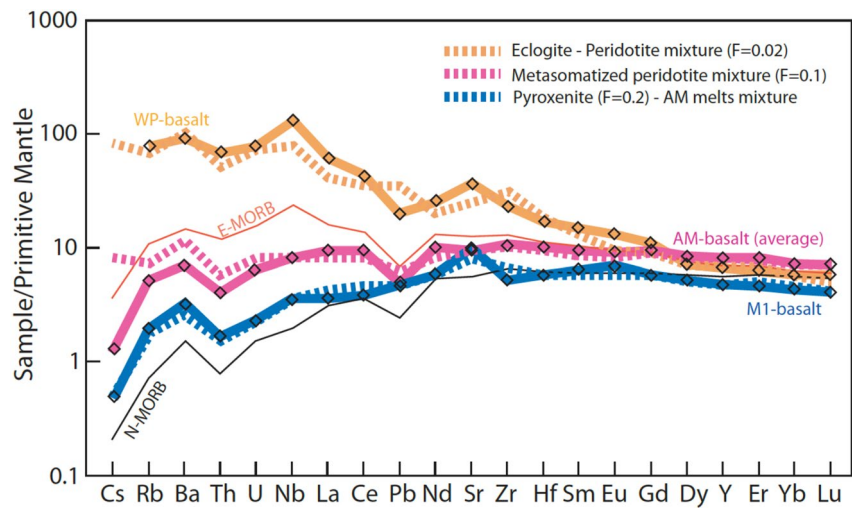


**Figure 9.** Incompatible trace element model. A spider diagram constructed from trace element mixing models normalized to the Primitive Mantle (McDonough & Sun, 1995). Thick solid lines correspond to the compositions of some of the analyzed samples: the average composition of AM-group basalts is represented in pink, a basalt sample from the Western Plateau is in orange, and an M1-group basalt is presented in blue. The thinnest lines represent E-MORB and N-MORB compositions in the study area, while the thick dashed lines correspond to our (best fit) models, attempting to reproduce the compositions of each of the selected samples. Model 1 (dashed orange line): A recycled eclogitic source with a composition of recycled upper crust (N-MORB) comprising 1% sediment (GLOSS) mixed with a spinel peridotitic source of depleted MORB mantle composition (3:2 mixing proportions), and the resulting source mixture melts at a low  $F = 0.02$  (non-modal fractional melting, Shaw, 1970). Model 2 (dashed pink line): A spinel-peridotitic source is mixed with 1% eclogitic melt derived from the model 1 source ( $F = 0.01$ ), and this metasomatized source melts at a higher  $F = 0.1$ . Model 3 (dashed blue line): A recycled pyroxenitic source of gabbroic composition melts with high  $F = 0.2$  and subsequent melt mixes (3:1 proportions) with average AM-basalt composition. Trace element composition and initial mineralogy used for each model can be found in Supporting Information S1 together with the melt/rock partition coefficients.

- Although scarce, few E-MORB were found in lavas erupted by either the X or Y-axes. These samples consistently possess more radiogenic Pb than samples of the AM, M1, M2, and N-MORB groups, and trend toward the HIMU component (Figure 3).

## 5.2. Significance of Coexisting Isotopic Variabilities

The large isotopic variability observed in our samples argues for a compositionally heterogeneous mantle source beneath the EPR. The hypothesis of a simple scenario, where a homogeneous “hotspot” source and the upper depleted mantle mix cannot fully explain the isotopic compositions of the North Orozco segment lavas. As previously mentioned, at least three main components are required to reproduce the global geochemical diversity of the northern EPR basalts, and more than three are required when considering the heterogeneity of the Mudskipper Seamounts. The Mudskipper Seamounts chain differs from the rest of the western off-axis magmatism (i.e., Northern Seamounts alignment and Western Plateau, Figure 1a) both in orientation and in the isotope signature of associated basalts. The Mudskipper Seamounts chain is orthogonal to the current ridge-axis, whereas the Northern Seamounts alignment is oblique, but they do intersect at the center of the ridge segment, which, in addition to an intensification of the magmatic budget suggests a higher degree of mantle heterogeneity below the studied area. The exceptional isotopic variability of MORB compositions observable in this  $\sim 15 \times 25$  km<sup>2</sup> of seafloor area confirmed this interpretation. As AM-type basalts represent mixtures between both the western enriched material (i.e., Western Plateau) and the depleted MORB mantle, the M1 and M2 components detected in the Mudskipper Seamounts are also present in the lavas from this EPR segment. Therefore, an important question that must be resolved is how are these mantle components connected, how did they get mixed together, and why has the isotopic variability been so well preserved in MORB samples collected inside such a small portion of seafloor?

At the first order, the balance between mantle heterogeneity and mixing processes directly controls the isotopic variability recorded by oceanic basalts. Mixing can occur either within the mantle by convection (solid-solid reactions), during melt transport (liquid-solid reactions) and/or inside the magma chamber (liquid-liquid interactions), and importantly any combination of these processes can also occur and/or co-exist. Reactive melt transport is not expected to create isotopic variations, but rather variations in elemental compositions. Another factor of variability to consider is whether the mantle is lithologically homogeneous or heterogeneous, as the petrology of the source, as well as the size of heterogeneities can influence the melting mode (i.e., melting as a single lithology or separated lithologies). A fine-scale heterogeneous mantle can melt as a single lithology despite that it is composed of distinct isotopic end-members. When melted, this type of heterogeneous mantle would generate a range of basalts with barely diverse isotopic compositions. On the contrary, when larger scale heterogeneities are preserved in the mantle source, the latter can melt preferentially and/or separately and create a more significant isotopic variability within the basalts.

While partial melting ( $F$ ) does not modify isotopic compositions directly it can have a selective impact on them (Niu & Hekinian, 2004; Niu et al., 1999), as distinct lithologies result in distinct solidi (i.e., peridotite vs. pyroxenite), and thus diverse melting behaviors. For example, low  $F$  melts usually sample more geochemically enriched and fertile materials, while higher  $F$  melts sample more geochemically depleted, and refractory mantle sources (Niu & Hekinian, 2004; Niu et al., 1999; Sobolev et al., 2005, 2007). Overall, the isotopic diversity of worldwide oceanic basalt compositions is commonly explained by invoking the melting and mixing of isotopically enriched pyroxenitic materials with depleted peridotitic melts (e.g., Brunelli et al., 2018; Dasgupta et al., 2010; Day et al., 2009; Hemond et al., 2006; Jackson & Dasgupta, 2008; Niu et al., 2002; Shorttle & MacLennan, 2011; Stracke et al., 1999; White, 2010). The geochemical imprint of such source heterogeneities is usually best preserved in regions where lower degree of partial melting prevail, whereas higher degree of melting favor the dilution of these signals at the benefit of that of the normal upper mantle (Niu et al., 1999, 2002). This difference explains why the isotopic variability of MORB from fast-spreading ridges is usually smaller compared to MORB from slow-spreading ridges (Batiza, 1984). Similar observations have been made between ridges (higher  $F$ , lower chemical variability) and neighboring seamounts (lower  $F$ , higher chemical variability) (Anderson et al., 2021; Niu & Batiza, 1997; Niu et al., 2002; Zindler et al., 1984), as well as within ocean island basalts whose amplitude of isotopic variability appears to be correlated to the volume of lava that was erupted (Chauvel et al., 2012). Recently, a mixing model involving fractional melts derived from a separated bi-lithological mantle source has also been proposed by Rudge et al. (2013). This model predicts the possibility of vast diversity in trace element compositions, as well as secondary isotopic mixing correlations that no longer reflect true end-member compositions (except for Pb-Pb isotopic space). Mallick et al. (2019) have since tested this model using trace element and isotope data obtained on MORB from the northern EPR region (including this study area) and ultimately came to the conclusion that this model does not apply in this study area.

Interestingly, the Northern Orozco ridge segment appears to be an exception. It displays a relatively fast spreading rate, a very high magmatic supply, has clear evidence for an axial magmatic chamber, and also the highest isotopic variability of the entire EPR. This higher variability is related to the presence of a nearby hotspot heterogeneous source (also responsible for the Mudskipper Seamounts, the Northern Seamounts and the Western Plateau), which introduced an additional degree of heterogeneity to the system. The increase over time of the magmatic supply below this ridge segment is also likely related to an increase in hotspot material inputs toward the ridge, rather than a progressive increase in the extent of melting below the ridge, as a change in the melting rate over time would have affected incompatible trace element concentrations and ratios, which is not observed here. Trace element patterns and concentrations (except for two samples) within AM-type basalts along the transversal profile are relatively homogeneous (Figure 4). The most primitive AM-type basalts (~8 wt% MgO) display similar trace element patterns and ratios whether they belong to the X, Y, or Z domains. A further means to evaluate the effect of melting versus source heterogeneity is to compare the co-variations of incompatible trace elements with radiogenic isotopes (Figure 5). The  $[\text{La}/\text{Sm}]_N$  ratio is sensitive to variations in the extent of melting, because La is more incompatible than Sm, therefore, the  $[\text{La}/\text{Sm}]_N$  ratio will decrease as the extent of melting increases, and conversely. While, radiogenic isotopes are used as a proxy for mantle heterogeneity, Figure 5 illustrates that the  $[\text{La}/\text{Sm}]_N$  ratios of AM, M1, and M2-type basalts are consistently correlated with all four isotopic systems. This suggests that mantle heterogeneity and mixing processes control the composition of basalts from the 16°N segment, a result that is confirmed by major element compositions

(Figure 5).  $\text{CaO}/\text{Al}_2\text{O}_3$  and  $\text{K}_2\text{O}/\text{TiO}_2$  ratios appear to be correlated with radiogenic isotope signatures as well.  $\text{CaO}/\text{Al}_2\text{O}_3$  ratios display a slight horizontal dispersion for a given isotopic composition (not observed in the  $\text{K}_2\text{O}/\text{TiO}_2$  ratios), a trend that can be attributed to fractional crystallization processes. Nevertheless, the trends observed on Figure 5 again suggest that mantle source compositions and melt mixing prevail over shallow magmatic processes in controlling the major element content of lavas from this area.

Due to the absence of mantle rock samples, and the ubiquity of mixing processes in this region, it is impossible to directly constrain either the degree of partial melting, or primitive melt compositions, thus it is impossible to infer the lithology of mantle sources. Despite this, using simple models of melting and mixing, and testing various starting lithologies, values of  $F$ , and mixing proportions, can help to outline of a plausible scenario. Donnelly (2002) previously proposed that a mixture between low- $F$  ( $F = 0.02$ ) eclogitic melt and peridotitic melt ( $F = 0.1$ ) could reproduce the composition observed in the Western Plateau magmatism. Contrarily, the M1-group basalts are best explained by higher- $F$  ( $F = 0.10$ – $0.20$ ) melts mixtures between peridotitic and pyroxenitic materials (Mallick et al., 2019; Mougél et al., 2014). Additional similar mixing calculations are presented further in the discussion, but the question remains, how can these results be reconciled with the actual isotopic variability observed in the samples?

A clear dichotomy exists in the isotopic signals presented in Figure 7b. On the one hand, M1 and M2-influenced samples show high amplitude and “chaotic” isotopic variability. The vertical amplitude of the spikes visible in this figure reflects the amount of the M1 and/or M2 component that is mixed with the AM. We note that even “zero age” basalts show a wide range of compositions for both the M1 and M2-type basalts. Such large isotopic variability within samples of a given “isotopic group,” within short distances geographically, supports the idea of magma mixing and a short crustal residence time of melts in the axial magma chamber (i.e., high frequency of recharge and eruptions). Interestingly, basalts that belong to the M1 and M2 groups display on average higher MgO concentrations than the AM-type basalts. Their radiogenic isotope compositions also correlate with the MgO content (higher proportions of M1 or M2 = higher MgO content). This suggests that the primary melts extracted from the source of the Mudskipper Seamounts (i.e., M1 and M2 group basalts) were likely more primitive than the AM-group melts, and that they likely melted separately, and subsequently hybridized in the axial magma chamber. Moreover, in order to sustain the high amplitude and “chaotic” isotopic variability observed in the M1 and M2 samples, rapid melt-transport combined with a short crustal residence time had to be involved. The presence of shallow dyke swarms beneath the main axial through of the 16°N segment supports the idea of a more significant melt transfer toward the surface, ultimately resulting in a hypermagmatic segment (Szitkar et al., 2016).

On the other hand, the ambient mantle signal shows low amplitude and low frequency isotopic variability (Figure 7b), being relatively constant over the short term, but seems to vary periodically over longer periods of time (100–150 kyrs). Primarily, fluctuations in the AM signal likely reflect the variations between different proportions of enriched and depleted mantle components (i.e., the western magmatism source, and the depleted EPR mantle). The temporal periodicity of the AM signal has been evaluated using the Lomb and Scargle periodogram (e.g., Albarède, 1995; Lomb, 1976; Scargle, 1982) as presented in Figure 8. Periodograms are calculated by adjusting sine functions of samples’ Dc value (as a proxy for their age) to isotopic data, and plotting the squared norm value of these functions with respect to wavenumber (the inverse of the wavelength). The advantage of the periodogram over other Fourier techniques is its suitability to handle unequally spaced data (see Agranier et al., 2005 for details). Peaks whose power exceeds 1, are considered significant with a confidence level >90%. Here, all isotopic systems exhibit significant peaks around wavenumbers of  $\sim 20^\circ^{-1}$  and  $30^\circ^{-1}$ , which correspond to wavelengths of  $0.05^\circ$  and  $0.035^\circ$  respectively. These observations are in agreement with the apparent periodicity of the isotopic signals in AM samples as represented in Figures 7 and 8b. A conversion of these angular distances into durations (using an average half accretion rate of  $\sim 4.2$  cm/y) reveals a periodicity of  $\sim 125$  kyrs. Of note, a secondary peak also arises in some of the periodograms, for the wave number  $170^\circ^{-1}$ . This peak corresponding to a wavelength of about  $0.005^\circ$  likely reflects the average spacing between this studies sample locations ( $\sim 0.004^\circ$ ).

In summary, two very distinct types of variability co-occur in the same place and at the same time. AM-group basalts consist of a low amplitude and continuous periodic signal, whereas M1 and M2 basalts constitute a more episodic signal of higher and more variable amplitude. Thus, a central question becomes how to reconcile this dichotomy within a single comprehensive and consistent scenario.

The composition of AM-like basalts implies that the ambient mantle is more isotopically enriched under this ridge segment than it is under the other ridge segments located further north (Figure 2). Additionally, the isotopic compositions of AM-group basalts represent an intermediate between depleted “normal” mantle, and Western Plateau compositions (Figure 3). Therefore we can infer that the ambient mantle composition under this specific segment of the EPR likely reflects the local enrichment of the depleted MORB mantle source by enriched material from the west. Recycling of the upper oceanic crust in the form of eclogites was previously proposed for the origin of this hotspot material (Donnelly, 2002). Sobolev et al. (2000) also stated that eclogite lithology begins to melt at higher pressures than normal peridotites. As it melts, the authors predict that eclogitic melts can infiltrate and react with the surrounding peridotite, resulting in the formation of a metasomatized peridotite, whose melts would preserve some geochemical aspects of the original eclogitic component. Here we suggest that the ambient mantle below the North Orozco segment may be an example of just such a process (i.e., metasomatization of a depleted peridotitic mantle by isotopically enriched eclogitic melts), where two isotopically distinct components were mixed together within the mantle, resulting in the formation of a second-generation peridotite source. Note that the ambient mantle must have preserved fine-scale heterogeneities in order to generate the variations observed in the proportions of enriched versus depleted components in the ridge’s melting region (i.e., the AM-group isotopic signal). The absence of compositions similar to the Western Plateau basalts in the sample suit supports the idea that the enriched material was likely diluted within the depleted MORB mantle instead of melting separately; otherwise, an isotopic variability similar to that of the Mudskipper source groups’ basalts (M1 and M2) would have been expected.

Trace elements are a better tool than isotopes in order to track the involvement of various compositions and mineralogy of the mantle sources. Using relatively simple binary mixing models, and adjusting for melting and source parameters, it is possible to test whether a hypothetical scenario can reproduce the trace element signatures exhibited by our samples. Although these simplistic models do not reflect the true complexity observed in nature, they do allow a first-order sorting between hypotheses. To that end we created several models, the main purpose of which was to estimate whether or not the melting of a peridotitic mantle previously metasomatized by eclogitic melts (as discussed above) could account for the composition of the average AM-type basalt composition. In order to model this scenario, we defined the starting trace element compositions for the mantle sources and melting modes ( $F$ ,  $D_{\text{min/melt}}$ , mineralogy), and calculated the compositions of the mixtures. We considered two starting mantle end-members: (a) an eclogitic source with a recycled upper crust (N-MORB) containing 1% sediment (GLOSS) composition and (b) a spinel peridotitic source with a Depleted MORB mantle composition. Our results indicate that the composition of the Western Plateau basalt is best reproduced by a 3:2 mixture of eclogitic with peridotitic end-members, and a low degree of melting ( $F = 0.02$ ). Following these calculations, a metasomatized ambient mantle source was modeled using a spinel peridotite mantle hosting 1% eclogitic melt ( $F = 0.01$ ). Modeled melt from such a source ( $F = 0.1$ ) reproduced relatively well the average composition of AM-group basalts. Lastly, the Mudskipper Seamounts signature (M1) was best reproduced by separate source melting and mixing (3:1) of pyroxenitic ( $F = 0.2$ ) and AM melts. The average composition of AM-group basalts, that of M-type basalts (10PUB17-03), and that of the Western Plateau basalt (D42-1; Donnelly, 2002) are represented along with the corresponding best-fit results in Figure 9.

All together these results suggest that the average composition of AM-group basalts (T-MORB) is compatible with a two-step mixing and melting model, of eclogitic and peridotitic materials that led to the geochemical enrichment/fertilization of the local depleted mantle. The very low amount of eclogitic melt contained in the peridotitic matrix, combined with the relatively high degree of partial melting in the spinel stability field can account for by the absence of HREE depletion in erupted basalts, as well as an enrichment in the most incompatible elements. Overall, the trace element compositions of the M1 and M2-type basalts require different mantle source, a result that is consistent with the isotopic data.

At fast spreading ridges, the time-scale of recharge of axial magma chambers is typically decadal to centennial (Moore et al., 2014); whereas the residence time of magma in the chamber is centennial to millennial (Sims et al., 2002), and melt-extraction from the magma lens to the surface, can occur over periods as short as a few days (Zellmer et al., 2012). In contrast, source processes vary on longer timescales  $>1$  Myrs (Bonatti et al., 2003; Brandl et al., 2016). These processes include both thermal changes in the mantle and variations of the mantle’s composition entering the melting-zone, both of which control the composition of primary melts entering the magma chamber. Melting processes and compositional changes are also closely interrelated. For

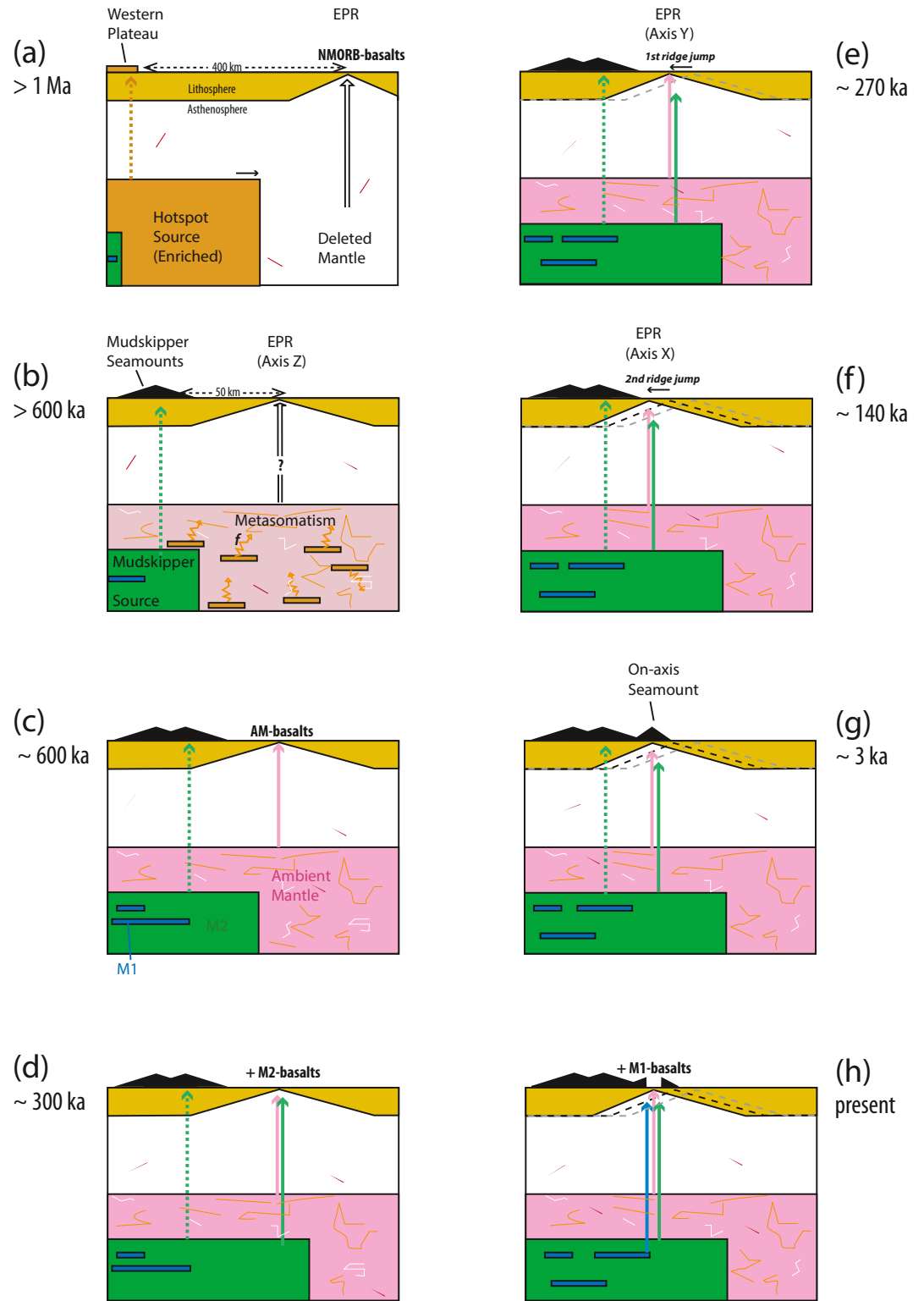


Figure 10.

example, on a time scale of several millions years, pulses of low-solidus temperature heterogeneities entering a ridge melting region can alone (i.e., at constant mantle temperature and spreading rate) dramatically decrease the degree of melting of the surrounding mantle (by latent fusion heat subtraction), consequently changing the volume and isotopic composition of MORB erupted, as well as the overall crustal thickness (Brunelli et al., 2018). Although this scenario is not considered to be of relevance in our case, it nevertheless illustrates the close co-dependence between mantle composition and melting. Over a 300-kyr-time interval, which is representative of the timescale investigated by this transversal sampling profile, it is very unlikely that the thermal structure of the mantle has varied significantly. Additionally, it is an insufficient period of time for the mantle in the melting column to be entirely restored (considering mantle upwelling rates and the spinel stability melting depth). Accordingly, we suggest that the periodicity of the isotopic signal observed in AM-samples is rather linked to specific mantle dynamics within the melting region, whose processes and durations (i.e., melt aggregation and transformations of mantle ascending through the melting column) are more compatible with the time-scale of the observed variations. Although the periodicity of this signal is of the same order as that observed by Cordier et al. (2010), we do not record high-amplitude spikes of enriched material. On the contrary, smooth and low amplitude alternations between enriched and depleted maximums are observed, which suggests a more continuous process, where fluctuations in the isotopic signal of the ambient mantle imply changes in the proportions of the two components involved inside the melting column. Periodic injections of more enriched material coupled with dynamic and continuous melting of a fine-grain scale heterogeneous source could provide such a mechanism (Kamenetsky & Maas, 2002) although it remains speculative. Essential parameters concerning source heterogeneity and melting are too poorly constrained or absent for a relevant quantitative approach to be attempted. Regardless, it remains possible to discuss the effect such a scenario might have on the composition of erupted basalts. The concept of a dynamic source combines both small-scale mantle heterogeneities with fractional melting models (Kamenetsky & Maas, 2002), and involves an assemblage of locally equilibrated mantle solids and related melt fractions evolving continuously during partial melting at mid ocean ridge. As melting begins, the production of low- $F$  enriched melts would increase at first, followed by the segregation and extraction of these melts, leaving a residue that would progressively produce higher- $F$  depleted melts, and so on. As the residual mantle migrates upward, replenishment at the bottom of the melting column would begin to occur. If pockets of enriched mantle periodically enter the melting region via the process described above, it could result in the generation of the sinusoidal variations observed on Figure 7 and examined in Figure 8. However, we speculate that such gradual isotopic variations would only be preserved in erupted melts, only if primary melts migrate fast and isolated across the melting region (i.e., high the porosity mantle channel; Kelemen et al., 1995), and crustal residence time is sufficiently short to avoid these melts being pooled.

### 5.3. Tentative Palinspastic Reconstruction

Ages as referred to in this section are not absolute ages, but rather constitute time boundaries extrapolated from former geophysical interpretations (bathymetric, magnetic, gravimetric and seismic) of the study area (Carbotte et al., 2000; Le Saout et al., 2014, 2018; Scheirer & Macdonald, 1995; Shah & Buck, 2006; Weiland & Macdonald, 1996). Altogether, the information provided by geochemical and geophysical data do allow us to propose a plausible scenario for the recent history of the 16°N EPR segment over the past 600 kyrs:

**Figure 10.** Tentative palinspastic reconstruction. (a) The East Pacific Rise and the “Mathematician Hotspot” do not interact yet. Western off-axis magmatism (i.e., the Western Plateau) is representative of the hotspot source, while further east, the ridge erupts typical depleted N-MORB basalts. (b) Depleted MORB mantle source becomes metasomatized by low- $F$  hotspot melts, ultimately forming a locally more enriched ambient mantle source below the North Orozco segment, while the Mudskipper Seamounts heterogeneous source begins to form seamounts close to the ridge. (c) The EPR begins to erupt AM-type basalts in association with a regional elevation and rugosity change of the seafloor along the ridge segment. In parallel, the Mudskipper Seamounts chain continues to develop eastward. (d) At this point, in addition to ambient mantle input, the Mudskipper Seamounts source (M2-type) is now being sampled on the ridge axis. These two sources initially melt separately and the respective melts mix in the axial magma chamber. (e) The first ridge jump occurs toward the Mudskipper Seamounts chain, and as a result, the morphology of the ridge changes due to the increase in the overall magmatic budget. The ridge continues to erupt AM-type basalts (and episodically some N-MORB and E-MORB). (f) The second westward ridge jump occurs, giving the EPR its current location and its inflated morphology. The isotopic signal registered in the AM-group basalt populations remains relatively constant, though small amplitude and frequency fluctuations are observed. (g) A seamount is erupted atop the current axis and is subsequently split symmetrically over the time. (h) Finally, in addition to the AM and M2-type basalts, a third component (M1-type) previously identified in the Mudskipper Seamounts source begins to be sampled at the current ridge axis.

1. Prior to 600 ka hotspot material metasomatized the depleted mantle forming a more enriched ambient mantle that preserved small-scale heterogeneities (Figure 10b).
2. About 600 ka, the EPR started to sample this more enriched source as recorded in the composition of the AM-type basalts. This represents the first geochemical evidence of the hotspot-ridge interaction (Figure 10c), which was also accompanied by a change in the morphology of the seafloor produced by this ridge segment (i.e., smoother and shallower than before), marked by the presence of ~600 ka bathymetric steps located on both sides of the ridge axis (Cormier et al., 1998).
3. Our results indicate that at about 300 ka, the Mudskipper Seamounts source was already feeding the ridge. This is supported by the presence of M2-type basalts erupted by the oldest portions of the relic axes, which are also present in the composition of the Mudskipper Seamounts (Figure 10d).
4. During the last 300 kyrs, the EPR jumped twice toward the Mudskipper Seamounts source (possibly 270 and 140 kyrs ago), resulting in a more and more robust and magmatic segment. During this time-period the ridge continued to produce AM-type lavas whose compositions fluctuated between the enriched and depleted isotopic end-members with an estimated periodicity of ~125 kyrs (Figures 10e and 10f).
5. The Mudskipper Seamounts, and the ridge, continued to converge until a seamount formed directly on the ridge axis. This structure was split in half and separated symmetrically on either side of the ridge over the last 3 kyrs (Figure 10g).
6. Very recently (likely during the last few centuries, Carlot et al., 2004), the M1 signature appears in the composition of basalts at the center of the segment at its widest part, coinciding alongside the intersection with the Mudskipper Seamounts (Figure 10h). In order to explain the isotopic variability that links the Mudskipper Seamounts source to that of the ambient mantle, separate melting of these two sources is now required, followed by mixing in the axial magma chamber accompanied by a short crustal residence time.

## 6. Conclusions

This study provides new high-resolution Sr-Nd-Hf-Pb radiogenic isotope, major, and trace element data for basaltic glass samples collected by submersible across the EPR axis of the North Orozco segment at ~15°4'N. First-order chronological assessment of our sampling profile sheds new light on the evolution and origin of the isotopic variability recorded in MORB samples from this area over the last ~320 kyrs. Notably, these new data confirm the extremely heterogeneous nature of the mantle under this region of the EPR, as suggested by previous studies. Our results both support and are consistent with an interaction between the EPR and a heterogeneous hotspot source. The remarkable isotopic variability in such a small area, despite fast-spreading ridge settings, also argue for a short crustal residence time of erupted magmas. Our interpretation of the across-axis profile has revealed two different modes of coexisting variability. The first of which is “high amplitude and discontinuous in time,” and is related to the recent influence of the Mudskipper Seamounts source on the ridge. This interaction is characterized by large isotopic variations between adjacent lavas whose wide range of compositions suggests varying proportions of the Mudskipper (M1 and M2-types) and the ambient mantle (AM) source components. These results argue strongly for an independent melting of these two sources followed by melt mixing in the axial magma chamber. The second type of variability revealed by our data is “low amplitude and low frequency,” has a periodicity of ~125 kyrs, and is only recorded in the AM-type basalts, whose isotopic signature is likely related to the early mixing of the Western Plateau-like enriched material (i.e., hotspot source) with the depleted MORB mantle. The isotopic composition of AM-type basalts depicts gradual and continuous isotopic fluctuations over time, alternating between enriched and depleted endmembers, that is most compatible with the melting of a single mixed source composed of two isotopically distinct components.

Finally, in addition to agreeing with current geophysical reconstructions, this study provides additional constraints on the evolution of the interaction between the EPR and the Mudskipper Seamounts. Our results suggest that before the first of the two-ridge jumps occurred ( $\geq 320$  ka), the ridge was already producing more enriched lavas compared to lavas erupted by adjacent EPR segments located further north. Additionally, we have shown that the source of the Mudskipper Seamounts was already interacting with the ridge at that time, and that the previously reported ancient gabbroic component present in this source is recorded at

the axis only since recently. Altogether, our results support a two-step hotspot-ridge interaction including a first stage of regional enrichment of the depleted ridge mantle by hotspot material; and a second involving mixing between ambient mantle melts and proximal melts from heterogeneous seamounts sourced nearby.

## Data Availability Statement

New data provided in this study can be found in Supporting Information S1, and are available online at EarthChem <https://doi.org/10.26022/IEDA/112071>. Other data used are indicated in the figure captions in which they appear with full information in the references section.

## Acknowledgments

B. Mougel, A. Agranier, C. Hemond, and P. Gente thank the RV L'Atalante crew and the Nautille team for the great work performed during the Cruise Parisub. B. Mougel, A. Agranier, and C. Hemond thank C. Bassoulet, P. Nonnotte, C. Liorzou, E. Ponzevera, and Y. Germain for their help during the analytical work. B. Mougel also thanks M. Le Saout for the interesting discussions about the magmatic activity and morphology of this ridge segment. A. Agranier and B. Mougel particularly thank A. Renouard for her precious help in the elaboration of the periodograms. They also warmly thank I. S. Foster for kindly accepting to read the latest version of the manuscript. Finally, B. Mougel, A. Agranier, C. Hemond, and P. Gente thank M. Perfit, Y. Niu, and a third anonymous reviewer, as well as the editor J. Blichert-Toft for the time spent on the manuscript, and their constructive and helpful comments. The analytical work was financially supported by the grant CNRS-INSU "PARISUB+" to A. Agranier. B. Mougel, A. Agranier, and C. Hemond also thank the Institut National des Sciences de l'Univers and Conseil Régional de Bretagne. B. Mougel thanks PAPIIT IA101519 and IA101521 for financial support.

## References

- Agranier, A., Blichert-Toft, J., Graham, D., Debaille, V., Schiano, P., & Albarede, F. (2005). The spectra of isotopic heterogeneities along the mid-Atlantic Ridge. *Earth and Planetary Science Letters*, 238(1–2), 96–109. <https://doi.org/10.1016/j.epsl.2005.07.011>
- Albarède, F. (1995). *Introduction to geochemical modeling*. Cambridge University Press.
- Anderson, M., Wanless, V. D., Perfit, M., Conrad, E., Gregg, P., Fornari, D., & Ridley, W. I. (2021). Extreme heterogeneity in mid-ocean ridge mantle revealed in lavas from the 8°20'N near-axis seamount chain. *Geochemistry, Geophysics, Geosystems*, 22(1), e2020GC009322. <https://doi.org/10.1029/2020gc009322>
- Batiza, R. (1984). Inverse relationship between Sr isotope diversity and rate of oceanic volcanism has implications for mantle heterogeneity. *Nature*, 309, 440–441. <https://doi.org/10.1038/309440a0>
- Batiza, R., Niu, Y. L., Karsten, J. L., Boger, W., Potts, E., Norby, L., & Butler, R. (1996). Steady and non-steady state magma chambers below the East Pacific Rise. *Geophysical Research Letters*, 23(3), 221–224. <https://doi.org/10.1029/95gl00016>
- Bender, J., Cormier, M., Langmuir, C., Shirey, S., & Donnelly, K., & PANRI Team. (1998). The East Pacific Rise and its flanks: New results between 15° and 19°N. *EOS*, 79, 832.
- Blichert-Toft, J., Agranier, A., Andres, M., Kingsley, R., Schilling, J. G., & Albarede, F. (2005). Geochemical segmentation of the Mid-Atlantic Ridge north of Iceland and ridge-hot spot interaction in the North Atlantic. *Geochemistry, Geophysics, Geosystems*, 6(1). <https://doi.org/10.1029/2004GC000788>
- Bonatti, E., Ligi, M., Brunelli, D., Cipriani, A., Fabretti, P., Ferrante, V., et al. (2003). Mantle thermal pulses below the Mid-Atlantic Ridge and temporal variations in the formation of oceanic lithosphere. *Nature*, 423(6939), 499–505. <https://doi.org/10.1038/nature01594>
- Brandl, P. A., Regelous, M., Beier, C., O'Neill, H. S. C., Nebel, O., & Haase, K. M. (2016). The timescales of magma evolution at mid-ocean ridges. *Lithos*, 240, 49–68. <https://doi.org/10.1016/j.lithos.2015.10.020>
- Brunelli, D., Cipriani, A., & Bonatti, E. (2018). Thermal effects of pyroxenites on mantle melting below mid-ocean ridges. *Nature Geoscience*, 11(7), 520–525. <https://doi.org/10.1038/s41561-018-0139-z>
- Carbotte, S., Mutter, C., Mutter, J., & Ponce-Correa, G. (1998). Influence of magma supply and spreading rate on crustal magma bodies and emplacement of the extrusive layer: Insights from the East Pacific Rise at lat 16°N. *Geology*, 26(5), 455–458. [https://doi.org/10.1130/0091-7613\(1998\)026<0455:iomsas>2.3.co;2](https://doi.org/10.1130/0091-7613(1998)026<0455:iomsas>2.3.co;2)
- Carbotte, S. M., Solomon, A., & Ponce-Correa, G. (2000). Evaluation of morphological indicators of magma supply and segmentation from a seismic reflection study of the East Pacific Rise 15°30'–17°N. *Journal of Geophysical Research: Solid Earth*, 105(B2), 2737–2759. <https://doi.org/10.1029/1999JB900245>
- Carlut, J., Cormier, M.-H., Kent, D. V., Donnelly, K. E., & Langmuir, C. H. (2004). Timing of volcanism along the northern East Pacific Rise based on paleointensity experiments on basaltic glasses. *Journal of Geophysical Research*, 109(B4). <https://doi.org/10.1029/2003JB002672>
- Castillo, P. R., Klein, E., Bender, J., Langmuir, C., Shirey, S., Batiza, R., & White, W. (2000). Petrology and Sr, Nd, and Pb isotope geochemistry of mid-ocean ridge basalt glasses from the 11°45'N to 15°00'N segment of the East Pacific Rise. *Geochemistry, Geophysics, Geosystems*, 1(11). <https://doi.org/10.1029/1999GC000024>
- Chauvel, C., Maury, R. C., Blais, S., Lewin, E., Guillou, H., Guille, G., et al. (2012). The size of plume heterogeneities constrained by Marquesas isotopic stripes. *Geochemistry, Geophysics, Geosystems*, 13(7). <https://doi.org/10.1029/2012GC004123>
- Cipriani, A., Brueckner, H. K., Bonatti, E., & Brunelli, D. (2004). Oceanic crust generated by elusive parents: Sr and Nd isotopes in basalt-peridotite pairs from the Mid-Atlantic Ridge. *Geology*, 32(8), 657–660. <https://doi.org/10.1130/G20560.1>
- Cordier, C., Benoit, M., Hemond, C., Dymont, J., Le Gall, B., Briais, A., & Kitazawa, M. (2010). Time scales of melt extraction revealed by distribution of lava composition across a ridge axis. *Geochemistry, Geophysics, Geosystems*, 11(7). <https://doi.org/10.1029/2010GC003074>
- Cormier, M.-H., Carbotte, S. M., & Gans, K. (1998). Magnetic and gravity study of the East Pacific Rise and its flanks at 12°–15°30'N: Ridge propagation, melt supply, and gravity rolls. *Eos, Transactions American Geophysical Union*, 79, S225.
- Cotten, J., Le Dez, A., Bau, M., Caroff, M., Maury, R. C., Dulski, P., et al. (1995). Origin of anomalous rare-earth element and yttrium enrichments in subaerially exposed basalts: Evidence from French Polynesia. *Chemical Geology*, 119, 115–138. [https://doi.org/10.1016/0009-2541\(94\)00102-e](https://doi.org/10.1016/0009-2541(94)00102-e)
- Dasgupta, R., Jackson, M. G., & Lee, C.-T. A. (2010). Major element chemistry of ocean island basalts—Conditions of mantle melting and heterogeneity of mantle source. *Earth and Planetary Science Letters*, 289(3), 377–392. <https://doi.org/10.1016/j.epsl.2009.11.027>
- Day, J. M. D., Pearson, D. G., Macpherson, C. G., Lowry, D., & Carracedo, J.-C. (2009). Pyroxenite-rich mantle formed by recycled oceanic lithosphere: Oxygen-osmium isotope evidence from Canary Island lavas. *Geology*, 37(6), 555–558. <https://doi.org/10.1130/G25613A.1>
- Donnelly, K. (2002). *The genesis of E-MORB: Extensions and limitations of the hot spot model* (PhD). Columbia University.
- Douglass, J., & Schilling, J.-G. (2000). Systematics of three-component, pseudo-binary mixing lines in 2D isotope ratio space representations and implications for mantle plume-ridge interaction. *Chemical Geology*, 163, 1–23. [https://doi.org/10.1016/S0009-2541\(99\)00070-4](https://doi.org/10.1016/S0009-2541(99)00070-4)
- Ferguson, D. J., Li, Y., Langmuir, C. H., Costa, K. M., McManus, J. F., Huybers, P., & Carbotte, S. M. (2017). A 65 k.y. time series from sediment-hosted glasses reveals rapid transitions in ocean ridge magmas. *Geology*, 45(6), 491–494. <https://doi.org/10.1130/G38752.1>
- Gill, J., Michael, P., Woodcock, J., Dreyer, B., Ramos, F., Clague, D., et al. (2016). Spatial and temporal scale of mantle enrichment at the Endeavour Segment, Juan de Fuca Ridge. *Journal of Petrology*, 57(5), 863–896. <https://doi.org/10.1093/ptrology/egw024>



- Hart, S., Hauri, E., Oschmann, L., & Whitehead, J. (1992). Mantle plumes and entrainment: Isotopic evidence. *Science*, 256, 517–520. <https://doi.org/10.1126/science.256.5056.517>
- Hemond, C., Hofmann, A., Heusser, G., Condomines, M., Raczek, I., & Rhodes, J. (1994). U-Th-Ra systematics in Kilauea and Mauna-Loa basalts, Hawaii. *Chemical Geology*, 116(3–4), 163–180. [https://doi.org/10.1016/0009-2541\(94\)90012-4](https://doi.org/10.1016/0009-2541(94)90012-4)
- Hemond, C., Hofmann, A. W., Vlastelic, I., & Nauret, F. (2006). Origin of MORB enrichment and relative trace element compatibilities along the Mid-Atlantic Ridge between 10° and 24°N. *Geochemistry, Geophysics, Geosystems*, 7(12). <https://doi.org/10.1029/2006GC001317>
- Jackson, M. G., & Dasgupta, R. (2008). Compositions of HIMU, EM1, and EM2 from global trends between radiogenic isotopes and major elements in ocean island basalts. *Earth and Planetary Science Letters*, 276(1–2), 175–186. <https://doi.org/10.1016/j.epsl.2008.09.023>
- Kamenetsky, V. S., & Maas, R. (2002). Mantle-melt evolution (dynamic source) in the origin of a single MORB suite: A perspective from magnesian glasses of Macquarie Island. *Journal of Petrology*, 43(10), 1909–1922. <https://doi.org/10.1093/ptrology/43.10.1909>
- Kelemen, P., Shimizu, N., & Salters, V. (1995). Extraction of mid-ocean-ridge basalt from the upwelling mantle by focused flow of melt in dunite channels. *Nature*, 375(6534), 747–753. <https://doi.org/10.1038/375747a0>
- Langmuir, C., Bender, J., Donnelly, K., Shirey, S., Cormier, M., Baker, E., & PANR1 Team. (1998). Petrology of the East Pacific Rise North of Orozco transform fault. *EOS*, 79, 832.
- Le Saout, M. (2015). *Interaction dorsale point chaud: Influence sur les processus tectoniques et magmatiques à l'axe de la dorsale Est Pacifique*, 16°N (PhD). IUEM, UBO.
- Le Saout, M., Deschamps, A., Soule, S. A., & Gente, P. (2014). Segmentation and eruptive activity along the East Pacific Rise at 16°N, in relation with the nearby Mathematician hotspot. *Geochemistry, Geophysics, Geosystems*, 15(11), 4380–4399. <https://doi.org/10.1002/2014GC005560>
- Le Saout, M., Thibaud, R., & Gente, P. (2018). Detailed analysis of near tectonic features along the East Pacific Rise at 16°N, near the Mathematician Hot Spot. *Journal of Geophysical Research-Solid Earth*, 123(6), 4478–4499. <https://doi.org/10.1029/2017JB015301>
- Li, Z.-X. A., & Lee, C.-T. A. (2006). Geochemical investigation of serpentinized oceanic lithospheric mantle in the Feather River Ophiolite, California: Implications for the recycling rate of water by subduction. *Chemical Geology*, 235, 161–185. <https://doi.org/10.1016/j.chemgeo.2006.06.011>
- Lomb, N. R. (1976). Least-squares frequency analysis of unequally spaced data. *Astrophysics and Space Science*, 39, 447–462. <https://doi.org/10.1007/bf00648343>
- Lundstrom, C. C. (2003). Uranium-series disequilibria in mid-ocean ridge basalts: Observations and models of basalt genesis. In B. Bourdon, G. M. Henderson, C. C. Lundstrom, & S. P. Turner (Eds.), *Uranium-series geochemistry* (Vol. 52, pp. 175–214). Mineralogical Society of America & Geochemical Society. <https://doi.org/10.1515/9781501509308-010>
- Macdonald, K., Fox, P., Miller, S., Carbotte, S., Edwards, M., Eisen, M., et al. (1992). The East Pacific Rise and its flanks 8–18°N: History of segmentation, propagation and spreading direction based on SeaMARC II and Sea Beam studies. *Marine Geophysical Researches*, 14(4), 299–344. <https://doi.org/10.1007/BF01203621>
- Mallick, S., Salters, V. J. M., & Langmuir, C. H. (2019). Geochemical variability along the northern East Pacific Rise: Coincident source composition and ridge segmentation. *Geochemistry, Geophysics, Geosystems*, 20(4), 1889–1911. <https://doi.org/10.1029/2019GC008287>
- Mammerickx, J., & Klitgord, K. D. (1982). Northern East Pacific Rise: Evolution from 25 m.y. B.P. to the present. *Journal of Geophysical Research*, 87(B8), 6751–6759. <https://doi.org/10.1029/JB087iB08p06751>
- McDonough, W. F., & Sun, S.-S. (1995). Composition of the Earth. *Chemical Geology*, 120, 223–253. [https://doi.org/10.1016/0009-2541\(94\)00140-4](https://doi.org/10.1016/0009-2541(94)00140-4)
- Meyzen, C. M., Blichert-Toft, J., Ludden, J. N., Humler, E., Mevel, C., & Albarede, F. (2007). Isotopic portrayal of the Earth's upper mantle flow field. *Nature*, 447(7148), 1069–1074. <https://doi.org/10.1038/nature05920>
- Moore, A., Coogan, L. A., Costa, F., & Perfit, M. R. (2014). Primitive melt replenishment and crystal-mush disaggregation in the weeks preceding the 2005–2006 eruption 9°50'N, EPR. *Earth and Planetary Science Letters*, 403, 15–26. <https://doi.org/10.1016/j.epsl.2014.06.015>
- Mougel, B., Agranier, A., Hemond, C., & Gente, P. (2014). A highly unradiogenic lead isotopic signature revealed by volcanic rocks from the East Pacific Rise. *Nature Communications*, 5, 4474. <https://doi.org/10.1038/ncomms5474>
- Mougel, B., Moreira, M., & Agranier, A. (2015). A “high He-4/He-3” mantle material detected under the East Pacific Rise (15°4'N). *Geophysical Research Letters*, 42(5), 1375–1383. <https://doi.org/10.1002/2014GL062921>
- Moynier, F., Agranier, A., Hezel, D. C., & Bouvier, A. (2010). Sr stable isotope composition of Earth, the Moon, Mars, Vesta and meteorites. *Earth and Planetary Science Letters*, 300(3–4), 359–366. <https://doi.org/10.1016/j.epsl.2010.10.017>
- Müller, R. D., Sdrolias, M., Gaina, C., & Roest, W. R. (2008). Age, spreading rates, and spreading asymmetry of the world's ocean crust. *Geochemistry, Geophysics, Geosystems*, 9(4). <https://doi.org/10.1029/2007GC001743>
- Niu, Y., & Batiza, R. (1997). Trace element evidence from seamounts for recycled oceanic crust in the Eastern Pacific mantle. *Earth and Planetary Science Letters*, 148, 471–483. [https://doi.org/10.1016/S0012-821X\(97\)00048-4](https://doi.org/10.1016/S0012-821X(97)00048-4)
- Niu, Y., Collerson, K. D., Batiza, R., Wendt, I. J., & Regelous, M. (1999). Origin of enriched-type mid-ocean ridge basalt at ridges far from mantle plumes: The East Pacific Rise at 11°20'N. *Journal of Geophysical Research*, 104(B4), 7067–7087. <https://doi.org/10.1029/1998JB900037>
- Niu, Y., & Hekinian, R. (2004). Ridge suction drives plume-ridge interactions (Chapter 9). In R. Hekinian & P. Stoffers (Eds.), *Oceanic hotspots* (pp. 285–307). Springer-Verlag. [https://doi.org/10.1007/978-3-642-18782-7\\_10](https://doi.org/10.1007/978-3-642-18782-7_10)
- Niu, Y. L., Regelous, M., Wendt, I. J., Batiza, R., & O'Hara, M. J. (2002). Geochemistry of near-EPR seamounts: Importance of source vs. process and the origin of enriched mantle component. *Earth and Planetary Science Letters*, 199, 327–345. [https://doi.org/10.1016/S0012-821X\(02\)00591-5](https://doi.org/10.1016/S0012-821X(02)00591-5)
- Peate, D. W., & Hawkesworth, C. J. (2005). U series disequilibria: Insights into mantle melting and the timescales of magma differentiation. *Reviews of Geophysics*, 43(1), RG1003. <https://doi.org/10.1029/2004RG000154>
- Perfit, M. R., Fornari, D. J., Smith, M. C., Bender, J. F., Langmuir, C. H., & Haymon, R. M. (1994). Small-scale spatial and temporal variations in mid-ocean ridge crest magmatic processes. *Geology*, 22(4), 375–379. [https://doi.org/10.1130/0091-7613\(1994\)022<0375:ssatv>2.3.co;2](https://doi.org/10.1130/0091-7613(1994)022<0375:ssatv>2.3.co;2)
- Regelous, M., Niu, Y., Wendt, I. J., Batiza, R., Greig, A., & Collerson, K. D. (1999). Variations in the geochemistry of magmatism on the East Pacific Rise at 10°30'N since 800 ka. *Earth and Planetary Science Letters*, 168(1), 45–63. [https://doi.org/10.1016/S0012-821X\(99\)00048-5](https://doi.org/10.1016/S0012-821X(99)00048-5)
- Reynolds, J., Langmuir, C., Bender, J., Kastens, K., & Ryan, W. (1992). Spatial and temporal variability in the geochemistry of basalts from the East Pacific Rise. *Nature*, 359(6395), 493–499. <https://doi.org/10.1038/359493a0>
- Rudge, J. F., Maclennan, J., & Stracke, A. (2013). The geochemical consequences of mixing melts from a heterogeneous mantle. *Geochimica et Cosmochimica Acta*, 114, 112–143. <https://doi.org/10.1016/j.gca.2013.03.042>

- Scargle, J. D. (1982). Studies in astronomical time series analysis. II. Statistical aspects of spectral analysis of unevenly spaced data. *The Astrophysical Journal*, *263*, 835–853. <https://doi.org/10.1086/160554>
- Scheirer, D. S., & Macdonald, K. C. (1995). Near-axis seamounts on the flanks of the East Pacific Rise, 8°N to 17°N. *Journal of Geophysical Research*, *100*(B2), 2239–2259. <https://doi.org/10.1029/94JB02769>
- Shah, A. K., & Buck, W. R. (2006). The rise and fall of axial highs during ridge jumps. *Journal of Geophysical Research: Solid Earth*, *111*(B8), B08101. <https://doi.org/10.1029/2005JB003657>
- Shaw, D. (1970). Trace element fractionation during anatexis. *Geochimica et Cosmochimica Acta*, *34*, 237–243. [https://doi.org/10.1016/0016-7037\(70\)90009-8](https://doi.org/10.1016/0016-7037(70)90009-8)
- Shorttle, O., & MacLennan, J. (2011). Compositional trends of Icelandic basalts: Implications for short-length scale lithological heterogeneity in mantle plumes. *Geochemistry, Geophysics, Geosystems*, *12*(11). <https://doi.org/10.1029/2011GC003748>
- Sims, K. W. W., Blichert-Toft, J., Fornari, D. J., Perfit, M. R., Goldstein, S. J., Johnson, P., et al. (2003). Aberrant youth: Chemical and isotopic constraints on the origin of off-axis lavas from the East Pacific Rise, 9°–10°N. *Geochemistry, Geophysics, Geosystems*, *4*(10). <https://doi.org/10.1029/2002gc000443>
- Sims, K. W. W., Goldstein, S. J., Blichert-Toft, J., Perfit, M. R., Kelemen, P., Fornari, D. J., et al. (2002). Chemical and isotopic constraints on the generation and transport of magma beneath the East Pacific Rise. *Geochimica et Cosmochimica Acta*, *66*(19), 3481–3504. [https://doi.org/10.1016/S0016-7037\(02\)00909-2](https://doi.org/10.1016/S0016-7037(02)00909-2)
- Sobolev, A. V., Hofmann, A. W., Kuzmin, D. V., Yaxley, G. M., Arndt, N. T., Chung, S.-L., et al. (2007). The amount of recycled crust in sources of mantle-derived melts. *Science*, *316*(5823), 412–417. <https://doi.org/10.1126/science.1138113>
- Sobolev, A. V., Hofmann, A. W., & Nikogosian, I. K. (2000). Recycled oceanic crust observed in “ghost plagioclase” within the source of Mauna Loa lavas. *Nature*, *404*(6781), 986–990. <https://doi.org/10.1038/35010098>
- Sobolev, A. V., Hofmann, A. W., Sobolev, S. V., & Nikogosian, I. K. (2005). An olivine-free mantle source of Hawaiian shield basalts. *Nature*, *434*(7033), 590–597. <https://doi.org/10.1038/nature03411>
- Soule, S. A., Fornari, D. J., Perfit, M. R., Tivey, M. A., Ridley, W. I., & Schouten, H. (2005). Channelized lava flows at the East Pacific Rise crest 9°–10°N: The importance of off-axis lava transport in developing the architecture of young oceanic crust. *Geochemistry, Geophysics, Geosystems*, *6*(8). <https://doi.org/10.1029/2005gc000912>
- Stracke, A., Salters, V. J. M., & Sims, K. W. W. (1999). Assessing the presence of garnet-pyroxenite in the mantle sources of basalts through combined hafnium-neodymium-thorium isotope systematics. *Geochemistry, Geophysics, Geosystems*, *1*(12). <https://doi.org/10.1029/1999GC000013>
- Szitkar, F., Dyment, J., Le Saout, M., Honsho, C., & Gente, P. (2016). Dyking at EPR 16°N hypermagmatic ridge segment: Insights from near-seafloor magnetics. *Earth and Planetary Science Letters*, *453*, 288–297. <https://doi.org/10.1016/j.epsl.2016.08.020>
- Turner, S., Beier, C., Niu, Y., & Cook, C. (2011). U-Th-Ra disequilibria and the extent of off-axis volcanism across the East Pacific Rise at 9°30'N, 10°30'N, and 11°20'N. *Geochemistry, Geophysics, Geosystems*, *12*(7). <https://doi.org/10.1029/2010gc003403>
- Waters, C. L., Sims, K. W., Perfit, M. R., Blichert-Toft, J., & Blusztajn, J. (2011). Perspective on the genesis of E-MORB from chemical and isotopic heterogeneity at 9–10°N East Pacific Rise. *Journal of Petrology*, *52*(3), 565–602. <https://doi.org/10.1093/ptrology/egq091>
- Weiland, C. M., & Macdonald, K. C. (1996). Geophysical study of the East Pacific Rise 15°N–17°N: An unusually robust segment. *Journal of Geophysical Research: Solid Earth*, *101*(B9), 20257–20273. <https://doi.org/10.1029/96JB01756>
- Wendt, J. I., Regelous, M., Niu, Y., Hékinian, R., & Collerson, K. D. (1999). Geochemistry of lavas from the Garrett Transform Fault: Insights into mantle heterogeneity beneath the eastern Pacific. *Earth and Planetary Science Letters*, *173*, 271–284. [https://doi.org/10.1016/S0012-821X\(99\)00236-8](https://doi.org/10.1016/S0012-821X(99)00236-8)
- White, W. M. (2010). Oceanic island basalts and mantle plumes: The geochemical perspective. In R. Jeanloz & K. H. Freeman (Eds.), *Annual Review of Earth and Planetary Sciences* (Vol. 38, pp. 133–160). Annual Reviews.
- Zellmer, G. F., Dulski, P., Iizuka, Y., & Perfit, M. R. (2012). Rates and processes of crystallization in on-axis and off-axis MOR basaltic melts. *Lithos*, *154*, 1–15. <https://doi.org/10.1016/j.lithos.2012.07.019>
- Zindler, A., Staudigel, H., & Batiza, R. (1984). Isotope and trace-element geochemistry of young Pacific seamounts: Implications for the scale of upper mantle heterogeneity. *Earth and Planetary Science Letters*, *70*, 175–195. [https://doi.org/10.1016/0012-821x\(84\)90004-9](https://doi.org/10.1016/0012-821x(84)90004-9)
- Zou, H., Zindler, A., & Niu, Y. (2002). Constraints on melt movement beneath the East Pacific Rise from <sup>230</sup>Th–<sup>238</sup>U disequilibrium. *Science*, *295*(5552), 107–110. <https://doi.org/10.1126/science.1064295>

## References From the Supporting Information

- Agranier, A., Blichert-Toft, J., Graham, D., Debaille, V., Schiano, P., & Albarede, F. (2005). The spectra of isotopic heterogeneities along the mid-Atlantic Ridge. *Earth and Planetary Science Letters*, *238*(1–2), 96–109. <https://doi.org/10.1016/j.epsl.2005.07.011>
- Donnelly, K. (2002). *The genesis of E-MORB: Extensions and limitations of the hot spot model* (PhD). Columbia University.
- Malaviarachchi, S. P. K., Makishima, A., & Nakamura, E. (2010). Melt-peridotite reactions and fluid metasomatism in the upper mantle, revealed from the geochemistry of peridotite and gabbro from the Horoman peridotite massif, Japan. *Journal of Petrology*, *51*, 1417–1445.
- Meyzen, C. M., Blichert-Toft, J., Ludden, J. N., Humler, E., Mevel, C., & Albarede, F. (2007). Isotopic portrayal of the Earth's upper mantle flow field. *Nature*, *447*(7148), 1069–1074. <https://doi.org/10.1038/nature05920>
- Mougel, B., Agranier, A., Hemond, C., & Gente, P. (2014). A highly unradiogenic lead isotopic signature revealed by volcanic rocks from the East Pacific Rise. *Nature Communications*, *5*, 4474. <https://doi.org/10.1038/ncomms5474>
- Plank, T., & Langmuir, C. H. (1998). The chemical composition of subducting sediment and its consequences for the crust and mantle. *Chemical Geology*, *145*, 325–394.
- Stracke, A., Bizimis, M., & Salters, V. J. M. (2003). Recycling oceanic crust: Quantitative constraints. *Geochemistry, Geophysics, Geosystems*, *4*(3). <https://doi.org/10.1029/2001GC000223>
- Sun, S.-S., & McDonough, W. F. (1989). Chemical and isotopic systematics of oceanic basalts: Implications for mantle composition and processes. *Geological Society London Special Publications*, *42*(1), 313–345.